Contrib Mineral Petrol (2015) 169:15
DOI 10.1007/s00410-015-1112-0

ORIGINAL PAPER

The Blacktail Creek Tuff: an analytical and experimental study of rhyolites from the Heise volcanic field, Yellowstone hotspot system

Torsten Bolte · Francois Holtz · Renat Almeev · Barbara Nash

Received: 7 August 2014 / Accepted: 9 January 2015 / Published online: 1 February 2015

Abstract The magma storage conditions of the 6.62 Ma Blacktail Creek Tuff eruption, belonging to the Heise volcanic field (6.62–4.45 Ma old) of the Yellowstone hotspot system, have been investigated by combining thermobarometric and experimental approaches. The results from different geothermometers (e.g., Fe–Ti oxides, feldspar pairs, apatite and zircon solubility, and Ti in quartz) indicate a pre-eruptive temperature in the range 825–875 °C. The temperature estimated using two-pyroxene pairs varies in a range of 810–950 °C, but the pyroxenes are probably not in equilibrium with each other, and the analytical results of melt inclusion in pyroxenes indicate a complex history for clinopyroxene, which hosts two compositionally different inclusion types. One natural Blacktail Creek Tuff rock sample has been used to determine experimentally the equilibrium phase assemblages in the pressure range 100–500 MPa and a water activity range 0.1–1.0. The experiments have been performed at fluid-present conditions, with a fluid phase composed of H_2O and CO_2, as well as at fluid-absent conditions. The stability of the quartzo-feldspathic phases is similar in both types of experiments, but the presence of mafic minerals such as biotite and clinopyroxene is strongly dependent on the experimental approach. Possible explanations are given for this discrepancy which may have strong impacts on the choice of appropriate experimental approaches for the determination of magma storage conditions. The comparison of the composition of natural phases and of experimentally synthesized phases confirms magma storage temperatures of 845–875 °C. Melt water contents of 1.5–2.5 wt% H_2O are required to reproduce the natural Blacktail Creek Tuff mineral assemblage at these temperatures. Using the Ti-in-quartz barometer and the Qz–Ab–Or proportions of natural matrix glasses, coexisting with quartz, plagioclase and sanidine, the depth of magma storage is estimated to be in a pressure range between 130 and 250 MPa.

Keywords Rhyolite · Yellowstone hotspot · Heise · Snake River Plain · Thermobarometry · Phase equilibria · Magma storage conditions

Introduction

Rhyolitic volcanism related to the track of the Yellowstone hotspot along the Snake River Plain in Idaho, USA, is the focus of a large number of studies, beginning with the descriptions of the voluminous volcanism of the central Snake River Plain by Bonnichsen (1982a, b) and Bonnichsen and Citron (1982) and ongoing with many studies on the petrology and geochemistry of the Yellowstone hotspot (e.g., Cathey and Nash 2004; Morgan and McIntosh 2005; Nash et al. 2006; Bindeman et al. 2007; Bonnichsen et al. 2008; Leeman et al. 2008; Cathey and Nash 2009; Girard and Stix 2009; McCurry and Rodgers 2009; Vazquez et al. 2009; Ellis et al. 2010; Girard and Stix 2010; Watts et al. 2011; Drew et al. 2013; and many others). However, a

Communicated by Jochen Hoefs.

Electronic supplementary material The online version of this article (doi:10.1007/s00410-015-1112-0) contains supplementary material, which is available to authorized users.

T. Bolte (✉) · F. Holtz · R. Almeev
Institute of Mineralogy, Leibniz University of Hannover,
Callinstraße 3, 30167 Hannover, Germany
e-mail: t.bolte@mineralogie.uni-hannover.de

B. Nash
Department of Geology and Geophysics, University of Utah, Salt
Lake City, UT 84112-011, USA

petrogenetic model for the formation of the rhyolites is still under debate. The continental crust has clearly contributed to the formation of Snake River Plain rhyolites, which is confirmed by isotopic and trace element compositions indicating a change in the magma source at the western edge of the Snake River Plain. This variation is marked by the transition from accreted oceanic terranes in the west to Precambrian basement in the east (Leeman et al. 1992), located in the western Idaho border region. On the other hand, Sr and Nd isotopic data preclude a simple partial melting of the Precambrian basement underlying much of the Yellowstone hotspot volcanic province (Nash et al. 2006; Leeman et al. 2008; Christiansen and McCurry 2008), and a contribution of mantle-derived mafic material needs to be taken into account.

The processes occurring in the crustal zones in which rhyolitic melts are assembled in magma reservoirs are also complex. For example, oxygen isotope data indicate that hydrothermal fluids modified the isotopic composition of rhyolite source materials probably during multiple caldera-forming cycles (Bindeman et al. 2007). The geochemistry of Snake River Plain rhyolites indicates that their compositions correspond to metaluminous ferroan granites following the classification proposed by Frost and Frost (2011). However, the products of single eruptive events and the evolution of volcanic rocks with time cannot be simply described by classical crystal fractionation of ferroan systems or by two member magma mixing processes (mafic–felsic). For example, the existence of different pyroxene populations in selected rhyolitic samples indicates that magma mixing or mingling of several rhyolitic batches occurred either at depth or during the eruptive process (Cathey and Nash 2009; Ellis et al. 2010).

The typical Snake River Plain anhydrous mineral assemblage is consistent with high magma temperatures. Using classical geothermometers (compositions of mineral pairs, zircon and apatite saturation), a general decrease in temperature with time has been observed over the history of the Yellowstone hotspot system. The earliest erupted silicic magmas in the western part of the Yellowstone hotspot province (16–17 Ma) were probably extremely hot—up to 1,080 °C (Perkins and Nash 2002). Temperatures in the central Snake River Plain, including the Bruneau–Jarbidge and Twin Falls eruptive centers, active between ~13 and 8 Ma, were typically in the range 900–1,000 °C (Honjo et al. 1992; Cathey and Nash 2004, 2009; Ellis et al. 2010; Almeev et al. 2012), whereas younger rhyolites (<7 Ma) in the eastern part (particularly Heise and Yellowstone) are more compositionally evolved and have lower pre-eruptive temperatures (typically 800–900 °C), and at Yellowstone, the 1.3 Ma Mesa Falls Tuff and the 0.64 Ma Lava Creek Tuff contain biotite and/or hornblende (Christiansen 2001; Watts et al. 2011), indicating a change in magma formation and/or storage conditions with time and space. In addition to temperature, one crucial parameter that needs to be determined to characterize magma storage conditions and eruptive mechanisms is the water content of the melts (H_2O_{melt}). From results in synthetic systems, H_2O_{melt} of high-temperature rhyolitic magmas can be extremely low because temperatures as high as 900–1,000 °C are close to the dry melting of quartzo-feldspathic systems. Results from Almeev et al. (2012) confirm this hypothesis, and H_2O_{melt} as low as 0.7–1.3 wt% H_2O for Snake River Plain high-temperature rhyolites from the Bruneau–Jarbidge eruptive center (950–975 °C) is realistic. With decreasing temperature, silicate melts can only be stable at higher H_2O_{melt} (Holtz et al. 2001), and thus, H_2O_{melt} should be higher in the younger, lower-temperature magmas, particularly those including biotite (and hornblende) in the phase assemblage. Although much work has been conducted on Snake River Plain rhyolite magma, parameters such as depth of magma storage and H_2O_{melt}—which are crucial to the interpretation of eruptive mechanisms—are not well quantified for most eruptive units. This study is focused on the determination of the pre-eruptive conditions of the Blacktail Creek Tuff, which belongs to the younger Yellowstone hotspot magmas from the Heise volcanic field. Classical tools such as thermobarometry from mineral compositions, compositions of natural glasses and melt inclusions are used. The information from natural assemblages is complemented by the experimental determination of phase equilibria at high pressure and temperature (100–500 MPa; 680–900 °C) which is one of the methods commonly applied to constrain pre-eruptive conditions (e.g., Rutherford et al. 1985; Scaillet and Evans 1999; Holtz et al. 2005) and is well suited to constrain water activities and depth of magma storage.

Heise volcanic field

The Heise volcanic field, active from 6.6 to 4.5 Ma, is the second youngest of the eruptive centers of the Yellowstone hotspot system and is located west of the Yellowstone National Park at the eastern border of Idaho. The Heise field is a well-preserved, large nested caldera complex with a surface area of approximately 100 km × 100 km (Morgan and McIntosh 2005; Bindeman et al. 2007; Watts et al. 2011). Usually, Heise tuff exposures are densely welded ignimbrite (Branney et al. 2008). All Heise magmas are erupted through Archean crust, confirmed by the location of the Heise volcanic field 300 km east of the Sr 0.706 isopleth that defines the transition from Mesozoic accreted terranes on the west to the eastern Precambrian craton of North America (Farmer and DePaolo 1983; Fleck and Criss 1985).

The eruptive activity of the Heise volcanic center occurred in late Miocene and early Pliocene between 6.62 and 4.45 Ma. The 6.62 Ma Blacktail Creek Tuff, the initial large-volume eruption at the Heise eruptive center, launched the Heise cycle with a 1,200 km^3, caldera-forming eruption (Morgan and McIntosh 2005; Watts et al. 2011, this study). The Blacktail Creek Tuff is a densely welded, homogeneous ignimbrite with phenocryst contents up to 17 vol% and is in the focus of this study. Two intermediate caldera-forming eruptions, also in the eruption category (VEI 7 + 8), occurred at 6.27 Ma and 5.51 Ma, the 750 km^3 Walcott Tuff and the 300 km^3 Conant Creek Tuff. The 5.57 Ma Tuff of Wolverine Creek seems to be subordinate and characterized by non-welded deposits. The final eruption of the Heise caldera cycle was the Kilgore Tuff (1,800 km^3) which is characterized by a highly welded, phenocryst-poor ignimbrite. The crystal content is as low as ~1 %. Exposures of the 4.45 Ma Kilgore Tuff span ~20,000 km^2 across parts of Idaho, Montana and Wyoming, and range from <3 to >120 m thickness, with the thickest deposits located near the three inferred source vent areas along the northern and southern margins of the Kilgore caldera (Morgan and McIntosh 2005). It is emphasized that the time interval between each large-volume eruption of the Heise center increases from the oldest to the youngest events. The study of Watts et al. (2011) extended the Heise cycle by a group of post-Kilgore Tuff rhyolitic eruptions with minor volumes. These are the Juniper Buttes, Long Hollow, Indian Creek and Sheridan reservoir rhyolites, with ages down to 3.96 Ma. However, the following ~2 Ma are without any major eruptions until the onset of activity on the Yellowstone volcanic plateau to the east marked by eruption of the voluminous 2.11 Ma Huckleberry Ridge Tuff (Christiansen 2001; Ellis et al. 2012).

Investigated sample

One sample of the Blacktail Creek Tuff has been selected for detailed analytical and experimental studies. It is collected from the Blacktail Creek Tuff outflow facies at the shoreline of the Blacktail Creek Reservoir; the type section of this unit is well described in Morgan and McIntosh (2005). The investigated sample is a rhyolitic tuff composed predominantly of a welded glass matrix containing approximately 16 vol% of phenocrysts (Fig. 1) as determined by point counting (8,642 points in one thin section). The phenocryst assemblage consists of ~37.8 vol% plagioclase (Pl), ~18.1 vol% sanidine (Sa), ~33.7 vol% quartz (Qz), ~3.9 vol% augite (Aug), ~2.5 vol% pigeonite (Pgt) and ~4.0 vol% magnetite (Mag) and ilmenite (Ilm). Accessory minerals that have been identified are apatite (Ap) and zircon (Zrn) (abbreviations after Whitney and Evans 2010). One biotite (Bt) grain has been identified in the thin sections of the investigated sample, but the mineral is surrounded by a reaction rim and may not be representative of the magmatic assemblage prevailing in the magma chamber prior to eruption. Some minerals, especially oxides, pyroxenes as well as quartz grains exhibit rounded shapes which may indicate resorption. Fracturing of minerals, typical for explosive rhyolites, is widespread. Tectosilicates and augite also have abundant melt inclusions. The distribution of the phenocrysts is homogeneous in the starting material, which is confirmed by the separate whole-rock geochemical analyses of three fragments initially belonging to one large sample (Table 1). The bulk Zr content varies in the range of 292–323 ppm and the bulk Ba content ranges from 1,059 to 1,280 ppm (electronic supplement Table 2). The bulk major element geochemical composition of the investigated sample is given in Table 1.

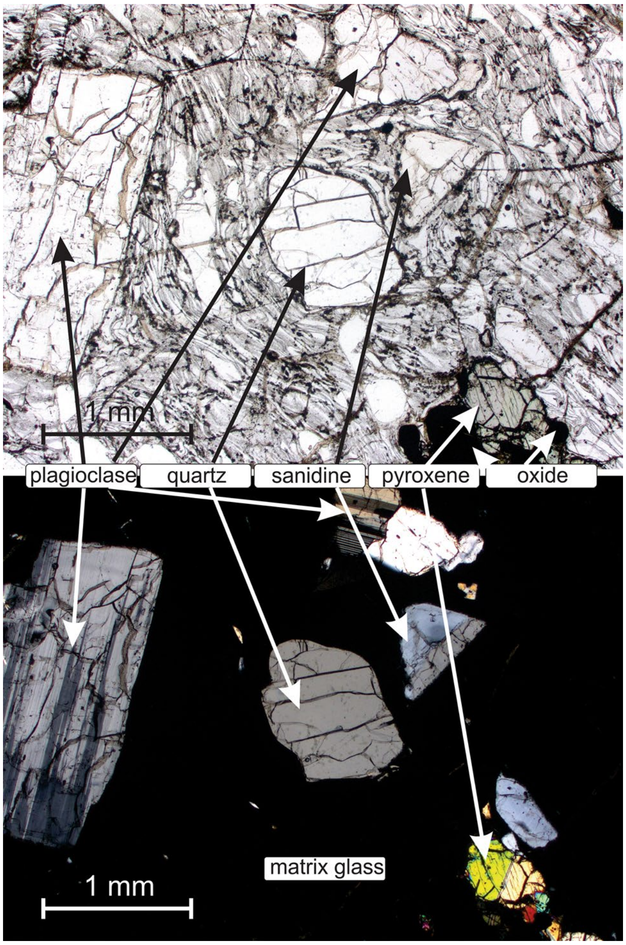

Fig. 1 Photomicrographs (non-polarized and polarized) of the natural sample Blacktail Creek Tuff used as starting material for the experiments and for natural phase analysis. The phases that can be observed are labeled

Experimental and analytical techniques

Crystallization experiments were performed using finely powdered glass made by melting ~70 g natural rock powder of the sample Blacktail Creek Tuff. This initial starting glass was prepared by three successive fusion steps performed in a Pt crucible at 1,600 °C and 1 atm in air for at least 3 h. Glass fragments collected from different parts of the glass block after the third fusion were analyzed separately by electron microprobe (see analytical methods), and the composition is identical within error (within the standard deviation). The average composition (162 analyses) is given in Table 1, and the data show that Fe and Na losses during fusion were minimal (Fe may form an alloy with Pt; Na may be lost in the gas phase in the furnace). The highest difference between bulk rock and experimental glass composition is observed for Al_2O_3 (Al_2O_3 in experimental glass is 0.3 wt% higher) and for FeO (value for experimental glass is 0.3 wt% lower). The starting glass contains minor amounts of Cl after fusion (~0.03 wt% Cl, the detection limit for Cl in glass measurements varies in the range of 75–100 ppm at 40-nA beam current).

The glass synthesized at 1 atm was crushed in a disk mill to a grain size <10 µm and was used for pre-hydration experiments. Pre-hydration experiments were conducted in an internally heated pressure vessel (IHPV) at 300 MPa and 1,050 °C in voluminous gold capsules (inner diameter: 8 mm at 3.5 cm length) to produce a high amount of homogeneous water-bearing glass for the following crystallization experiments. Three pre-hydration experiments were conducted in order to synthesize glasses containing approximately 1, 1.5 and 2.5 wt% H_2O. In addition, seven smaller glass samples containing 2.3–8.2 wt% H_2O were prepared at pressures above 500 MPa and 1,100 °C in Pt capsules to calibrate the determination of water concentrations by microprobe measurements.

Crystallization experiments were conducted in cold-seal pressure vessels (CSPV) pressurized with H_2O at 200 MPa and in a temperature range of 680–875 °C. The intrinsic redox conditions are near the nickel–nickel oxide buffer (hereafter labeled ~NNO) which are equivalent to the oxygen fugacity of the quartz–fayalite–magnetite solid oxygen buffer (hereafter labeled QFM) +1 log unit. Another set of experiments was conducted in an IHPV pressurized with a mixture of Ar and H_2 gases and equipped with a Shaw membrane (see Berndt et al. 2002 for description of the apparatus). IHPV experiments were conducted at 900 °C and at pressures of 100, 300 and 500 MPa. Considering that magnetite–ilmenite pairs from the Blacktail Creek Tuff indicate conditions close to the QFM buffer (see below), the amount of hydrogen added to the Ar pressure medium was chosen so that redox conditions of ~QFM are reached at water-saturated conditions. Hydrogen diffuses through the noble metal of the sample container (capsules), and in the presence of water, the oxygen fugacity is controlled by the equilibrium reaction of water formation ($H_2 + ½ O_2 \leftrightarrow H_2O$). As a result, at a given fH_2, the fO_2 decreases with decreasing water activity in the experimental charge. The fO_2 in the water-undersaturated experiments is lower than that in water-saturated experiments (see, for example, detailed discussion in Schuessler and Botcharnikov 2008) and can be estimated using the relation $\log fO_2 = \log fO_2$ (at $aH_2O = 1) \cdot aH_2O^2$ (Botcharnikov et al. 2005). We estimate that the overall error in the calculated fO_2 is about ~0.2 log units (Botcharnikov et al. 2005).

Most of the experiments were conducted at low water activities and high temperature (800–900 °C). Such conditions represent the most geologically relevant conditions because the rhyolites are devoid of hydrous minerals and geothermometry of Snake River Plain rhyolites predict temperatures above 800 °C (see below, e.g., Perkins and Nash 2002; Nash et al. 2006; Cathey and Nash 2004, 2009; Ellis et al. 2010; Watts et al. 2011). The starting prehydrated glasses or mixtures of two pre-hydrated glasses were used for the crystallization experiments in CSPV at 200 MPa (temperature range 680–875 °C) and in IHPV at 100 MPa (900 °C). The glasses were sealed in gold capsules (~15 mm length, 2.8 mm internal diameter and 0.2 mm wall thickness). For water-saturated experiments, 10 wt% H_2O was added to the dry glass powder. For water-undersaturated experiments, no additional volatile phase was added to the capsule. The amount of water in the prehydrated glasses was always lower than the water solubility at 200 MPa which is around 6 wt% H_2O in rhyolitic melts (Tuttle and Bowen 1958; Moore et al. 1998). Thus, in most of our 200 MPa water-undersaturated experiments, the conditions were fluid-absent and the prevailing water activity, aH_2O, can be determined from the amount of water present in the glasses after the experiment using the model of Burnham (1994). The experiments at 300 and 500 MPa in IPHV were conducted with dry glasses, and different amounts of water were added to the capsules. Water-undersaturated conditions were obtained by adding amounts of water which are lower than required for water saturation (<6.9 wt% for 300 MPa and <8.8 wt% for 500 MPa).

Some experiments were conducted at nominally dry conditions using dry glasses previously stored at 110 °C (no fluid added). It is emphasized that such experiments are not strictly water-free because (1) it is nearly impossible to avoid adsorbed water on the surface of the glass powder grains during the capsule preparation and (2) hydrogen of the pressure medium may diffuse through the noble metal capsules. Thus, in nominally dry experiments, a fluid phase was not present, but the silicate melts contained small amounts of water mainly dissolved as OH groups (~0.3–1.0 wt% depending on pressure).

A series of experiments at 200 MPa (765–875 °C) was also conducted at water-undersaturated conditions in the presence of a H_2O–CO_2-bearing volatile phase. For these experiments, pre-hydrated glasses and $Ag_2C_2O_4$ were sealed in Au capsules.

The run duration varied with temperature and was always more than 336 and up to 1,368 h for runs at 680–875 °C (CSPV experiments). Experiments at 900 °C were performed for at least 226 and up to 332 h. All experiments were performed by applying directly the desired temperature at isobaric conditions. Two-step experiments with a first stage at a superliquidus temperature were not performed to enhance the nucleation of crystals along the grain boundaries of initial glass fragments (e.g., Holtz et al. 1992). Maximal temperature variations during the experiments were ±5 °C. The CSPV experiments were cooled with a flux of compressed air, and the typical time needed to quench the samples down to ~400 °C is <3 min. Considering that the investigated compositions are high-silica rhyolites, this cooling rate is sufficient to avoid the formation of quench phases. The cooling rate in IHPV is faster than in CSPV.

Analytical methods

Electron microprobe

The natural phases (crystals, matrix glass and glass inclusions) and the experimental products were analyzed with a Cameca SX100 electron microprobe at the University of Hanover, Institute for Mineralogy. The major element composition of the mineral phases was analyzed using the following analytical conditions for crystalline phases: accelerating voltage of 15 kV, beam current of 15 nA, counting time 10 s on peak for all elements. Glasses were analyzed using a defocused beam (10-μm beam diameter) with 15 kV accelerating voltage and beam current of 4 or/and 15 nA. To avoid loss of Na and K, the counting time for these elements was reduced to 4 s at 15 nA. Hydrous glasses were double-checked by using both 4- and 15-nA beam current to quantify alkali losses. For calibration, internal standards as well as external standards were used for each microprobe session. A natural well-characterized rhyolite glass standard was used for dry glass calibrations, and pre-hydrated samples of natural Blacktail Creek Tuff have been applied for hydrous glass compositions (Electronic supplement Fig. 1). Lake County plagioclase for feldspars and Kakanui augite for pyroxenes were common standard samples as well. Ba, Mn, Zr, Cl, F, S and P in glasses were analyzed at a second beam condition with 40-nA beam current to improve the detection limit. Counting times varied from 10 to 30 s. For the measurements of Ti in quartz, the Ti peak was measured only on LPET analyzer crystal at 150 nA and a counting time of 360 s on peak to get high resolution of <13 ppm. Ti-in-quartz measurements were re-checked with standard sample material provided by Andreas Audetat applied in Huang and Audetat (2012). Special conditions given by Parat and Holtz (2005) were also used to analyze Cl, F and S in apatites.

In this study, the composition of glasses was used to estimate the depth of storage conditions using the proportions of quartz and feldspar components (Qz, Ab, An, Or). Therefore, the possible loss of alkalis in water-rich glasses must be controlled carefully. The microprobe settings for this study were checked and optimized, but loss of Na could not be avoided completely for some glasses containing more than 3 wt% H_2O. The loss of Na could be quantified by using calibration measurements on standard glasses with known Na_2O and H_2O contents but was only found to be serious for glasses with very high water contents (e.g., 8.8 wt% H_2O, synthesis at 500 MPa, loss of 1.3 wt% Na_2O absolute). Most experiments constraining the pre-eruptive conditions were made of glasses with 3 wt% H_2O or less, and corrections for Na loss were not applied.

In most experimental studies on crystallization of rhyolitic melts, the measurement of the composition of small crystals is a challenge. Microprobe measurements on crystals smaller than 2–3 μm always show contamination by elements from the surrounding glass. For the analyses with obvious high contamination, the analytical information was limited to the reporting of the presence of the mineral phase. For most titanomagnetite and for some pyroxene crystals, the crystal composition is recalculated by mass balance, excluding all non-stoichiometric elements (corrected compositions are specified in electronic supplement Table 4). If three or more measurements in one single experiment yielded the same result, even at different degrees of contamination, the values were used for the interpretations.

Analysis of water concentration in glasses

The exact determination of the water concentration in the glasses is crucial in this study considering that the natural systems are water-undersaturated and that water activity is one main parameter influencing phase stabilities and the crystal proportions. The water contents of the pre-hydrated glasses were determined by Karl Fischer titration (KFT) (for this method, see Behrens et al. 1996), and Fourier transform infrared spectroscopy (FTIR). The water contents of experimental glasses were determined by near-infrared (NIR) and mid-infrared (MIR) spectroscopy if a suitable amount of glass was available or was determined with the electron microprobe "by-difference." Detailed information of the apparatus is given in electronic supplementary A.

Molar absorption coefficients of 1.41 and 1.66 l cm^{-1} mol^{-1} for the 4,520 and 5,230 cm^{-1} bands, respectively, were used to calculate the total water contents from NIR measurements (coefficients were determined for rhyolitic glasses by Withers and Behrens 1999). The water contents for MIR measurements (3,550 cm^{-1}) were calculated using a molar absorption coefficient of 78 l cm^{-1} mol^{-1}. This value was determined from Snake River Plain rhyolitic glasses containing <2 wt% H_2O synthesized in experiments above the liquidus in which the water content was determined by Karl Fischer titration (Almeev et al. 2012). The value is slightly higher than most of the molar absorption coefficients mentioned in the literature ranging from 61 to 70 (Mandeville et al. 2002). However, the dataset published by Mandeville et al. (2002) does not contain data for high-silica rhyolites, and this dataset clearly shows that the molar absorption coefficient increases from basaltic to dacitic melts.

The water content of experimental glasses was also estimated using the classical "by-difference" method based on the sum of the EMPA, which has a relatively high uncertainty of ±0.5–0.7 wt% H_2O (e.g., Parat et al. 2008). In this study, we used pre-hydrated standard glasses with known water contents (2.3–8.2 wt% H_2O) determined by FTIR to calibrate the "by-difference" method. A representative calibration plot is given in electronic supplement Fig. 1, and such calibration plots were systematically established for each microprobe session. Using this method, the uncertainty, which corresponds to the standard deviation of the analyses, is estimated to be ±0.35 wt% H_2O.

Analytical results of Blacktail Creek Tuff sample

Geothermometry/Geobarometry

The individual analysis of mineral phases and matrix glass from the natural Blacktail Creek Tuff sample are given in the electronic supplement (electronic supplement Tables 1 and 2). The temperatures estimated from oxide pairs, pyroxene pairs and plagioclase pairs are summarized in Table 4. All measured mineral pairs were in direct contact with each other or exhibiting crystal intergrowth. The glass analyses were used to estimate temperature using plagioclase–melt compositions (Putirka 2008) and apatite and zircon solubility models (Harrison and Watson 1984; Watson and Harrison 1983).

The pyroxene compositions are shown in Fig. 3. Pigeonite components vary from $Fs_{44}Wo_3En_{53}$ to $Fs_{54}Wo_4En_{43}$. Augites are more homogeneous and vary from $Fs_{21}Wo_{41}En_{37}$ to $Fs_{24}Wo_{42}En_{34}$. The Fe/Mg ratio of augite is constant with a value of 0.6, whereas the Fe/Mg ratio of pigeonite varies in the range of 0.8–1.2. The mineral pair temperatures from pyroxenes (Aug–Pgt) calculated by QUILF (fixed at 200 MPa) range from 829 to 934 °C with high uncertainties up to 59 °C. Calculations of the temperature and oxygen fugacity (fO_2) were conducted by including the measured pyroxene components and a pressure fixed at 200 MPa. The used pairs are given in Table 4. It has to be mentioned that all pyroxene pairs were in direct contact with each other, except for the first pair in Table 4. The first pyroxene pair from Table 4 is an average value of all analyzed augites and pigeonites from the Blacktail Creek Tuff sample. In a second step, equilibrium temperatures were calculated by QUILF keeping χ_{En}, χ_{Wo} of one phase constant and pressure fixed at 200 MPa and allowing the program to calculate temperature, fO_2, χ_{En} and χ_{Wo} of the coexisting pyroxene. The calculated temperatures and oxygen fugacities are also given in Table 4. Although all analyzed pyroxene crystals do not show any obvious chemical zoning, temperatures calculated with fixed pigeonite components range from ~843 to ~955 °C and are significantly higher than temperatures calculated with fixed augite components ranging from ~825 to ~861 °C. The pairs (c) and (f) yield the best overlapping results with 860 and 839 °C for recalculated pigeonite composition and 857 and 843 °C for recalculated augite composition, respectively. Calculations according to Putirka (2008) yield lower temperatures (809–848 °C). The test for equilibrium using the calculated $KD_{(Fe–Mg)}$ values of pyroxenes (Putirka 2008) indicates that minerals do not lie along an equilibrium line. After Putirka (2008), the value of the $KD_{(Fe–Mg)}$ Aug/Pgt should be 1.09 ± 0.14, but the Fe/Mg values are significantly higher for pigeonite than for augite, resulting in $KD_{(Fe–Mg)}$ Aug/Pgt values <0.69. Assuming that the $KD_{(Fe–Mg)}$ melt/aug and $KD_{(Fe–Mg)}$ melt/Pgt should be similar, we checked our values with the dataset of Bédard (2010) for high-silica melts. Keeping in mind the low Fe and especially the low Mg contents for the natural Blacktail Creek Tuff glasses, we determined $KD_{(Fe–Mg)}$ melt/cpx in a range of 0.10–0.13 and $KD_{(Fe–Mg)}$ melt/Pgt in a range of 0.18–0.22. Published values for melt/cpx, summarized in Bédard 2010, range from 0.08 to 0.25. From the comparison with the dataset of Bédard (2010), we can conclude that pyroxene and melt compositions are within values usually observed in experiments. However, the low $KD_{(Fe–Mg)}$ Aug/Pgt value indicates that the temperatures estimated from pyroxene pairs need to be treated with caution.

The normative components of plagioclase vary from $Ab_{65}An_{30}Or_5$ to $Ab_{69}An_{22}Or_9$ and for sanidine from $Ab_{37}An_3Or_{57}Cls_3$ to $Ab_{46}An_2Or_{49}Cls_2$ (Fig. 4; Table 4), where Cls is the Celsian component ($BaAl_2Si_2O_8$). The calculated temperatures for feldspar pairs (plagioclase–sanidine) range from 830 to 861 °C. Generally the analyzed feldspars do not show any zonation in major element composition and are assumed to be homogenous. Pair

(e) (Table 4) only shows distinct zoning with higher An (+5 %) and lower Or (−2 %) contents in the core, resulting in a higher crystallization temperature for the core (+22 °C). Average compositions of seven crystal pairs (in contact or aggregated) were used for calculations. The scattering of temperatures may be affected by slight core-rim variations in major element compositions, depending on the cutting angle of the analyzed crystal. Plagioclase-liquid temperatures are slightly higher and range from 860 to 867 °C (both after Putirka 2008) (Fig. 4). The calculated temperatures given by the oxide geothermometers ILMAT and ilmenite–magnetite (Andersen et al. 1993; Lindsley 1983; Stormer 1983; Ghiorso and Evans 2008) range from 853 up to 895 °C for the three analyzed individual pairs. Calculations with average composition of all analyzed ilmenite and Ti-magnetite yield 865 °C (after Ghiorso and Evans 2008) and 854 °C following the calculation method of Andersen and Lindsley (1985). The calculated oxygen fugacity is in the range of log fO_2 −12.2 to −13.5 (~QFM) and corresponds with the average range obtained from pyroxene compositions varying from ~ −12.4 to −13.5. The Ti activity ($a\text{TiO}_2$) is at a relatively constant value of 0.54 ± 0.02. Temperatures estimated from the solubility models for apatite and zircon (Harrison and Watson 1984; Watson and Harrison 1983) are calculated for the bulk composition (Table 2) as well as for the single glass analyses (electronic supplement Table 1). Estimated temperatures for the glasses are 867 and 862 °C, respectively, and slightly higher than calculated for the bulk composition (~−15 °C for apatite solubility and ~−10 °C for zircon solubility). Keeping in mind the high uncertainty for P_2O_5 and ZrO_2 determined by microprobe (see standard deviation of microprobe analyses, Table 3 and electronic supplement Table 1), our results from glasses need to be interpreted with caution but are consistent with the results from bulk rock analyses. The zircon saturation temperature determined from the bulk rock composition for the sample investigated in this study (852 °C) is nearly identical to that determined by Watts et al. (2011) for the Blacktail Creek Tuff (848 °C).

Matrix glass and glass inclusions

Up to 14 individual glass shards have been analyzed (3–7 analysis each) to check for the homogeneity of the matrix glass (see average values in Table 2). No significant compositional variations are observed (Fig. 5). FeO and TiO_2 concentrations, which may reflect different degrees of differentiation, do not change significantly (Electronic supplement Table 1). The FeO contents are in the range of 0.99–1.42 wt%, but most glass shards have concentrations between 1.1 and 1.3 wt%. TiO_2 concentrations are in the range of 0.16–0.21 wt%.

The mineral phases of the Blacktail Creek Tuff rock sample are rich in glass inclusions (Fig. 2), especially in augite, feldspars and quartz. The results listed in Electronic supplement Table 5 show a wide range of glass compositions. Inclusions trapped in augites often show more evolved chemical compositions, with lower FeO contents than matrix glasses (Fig. 5). In contrast, inclusions in quartz and feldspars have the same compositional range as matrix glasses. Most inclusions in augite have higher K_2O concentrations than in the glass matrix as well as inclusions in quartz and feldspars. The results of CIPW norm calculations, given in Table 5, are plotted in the ternary Qz–Ab–Or diagram (Fig. 6) and confirm that several glass inclusions in augite are shifted toward the Qz–Or sideline of the ternary system. From the database obtained in this study, two separate populations of glass inclusions in augite may be distinguished. One population has high K and low Na; the second population has a compositional range similar to that of the matrix glass (Fig. 5). In several cases, both types of inclusions can be observed in a single mineral grain (see Electronic supplement Table 5). Different tests have been performed to check whether the two populations may result from analytical problems such as contamination by the host mineral during electron microprobe analysis. Binary oxide plots in which the composition of the host mineral was also reported clearly show that this is not the case. However, it cannot be excluded that some small daughter crystals other than the host mineral may have formed after entrapment in some inclusions.

Titanium in quartz

We applied the revised Ti-in-quartz thermobarometer of Huang and Audetat (2012) to estimate magma storage conditions, focusing on pressure determination. The equation of Huang and Audetat (2012) allows pressure to be determined whether temperature and the titanium activity ($a\text{TiO}_2$) in the system are fixed. The $a\text{TiO}_2$ of the Blacktail Creek Tuff magma system has been calculated by using the titanomagnetite–ilmenite geothermometer of Ghiorso and Evans (2008) and $a\text{TiO}_2 = 0.54 \pm 0.02$ (Electronic Supplement Table 6). The temperature range used for the pressure calculations was derived from the results of geothermometry (see above, Table 2). The Ti concentrations determined by microprobe in 14 quartz grains range from 141 to 181 ppm without any measureable zoning in individual quartz grains. The standard deviation for each grain is shown in Fig. 7 and Electronic Supplement Table 6. Considering a temperature range varying from 821 to 876 °C (average of pyroxene pairs and of oxide pairs, respectively), the estimated pressure range is 100–250 MPa. Since pressure is negatively correlated to temperature (at fixed $a\text{TiO}_2$), the estimated pressures are the lowest for the temperature estimated from pyroxene pairs.

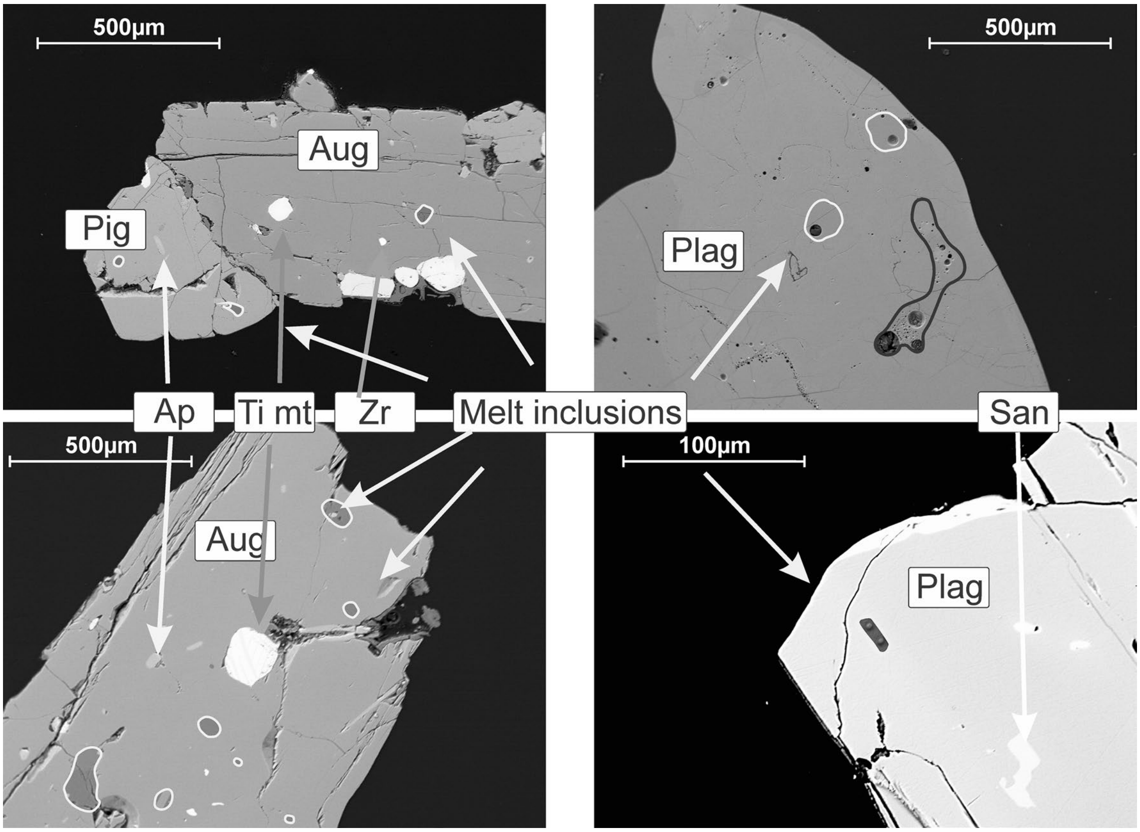

Fig. 2 Backscattered electron images of picked natural Blacktail Creek Tuff phases as labeled. *Ti-Mag* titanomagnetite, *Aug* augite, *Pgt* pigeonite, *Pl* plagioclase, *Sa* sanidine, *Ap* apatite, *Zrn* zircon. Observable glass inclusions are surrounded with a *white line*. In some cases, the penetration of the microprobe beam is visible

Table 1 Chemical composition of Blacktail Creek Tuff bulk and glasses normalized to 100 %

Sample		SiO_2	TiO_2	Al_2O_3	FeO	MnO	MgO	CaO	BaO	Na_2O	K_2O	P_2O_5	ZrO_2	Cl	Total of analysis
Bulk (09_018)	wt% ox	74.57	0.30	12.82	2.25	0.05	0.25	1.14	0.12	3.12	5.26	0.08	0.04		97.23
Bulk (BCT 1)	wt% ox	74.49	0.31	12.90	2.25	0.05	0.29	1.28	0.14	3.12	5.08	0.04	0.04		97.49
Bulk (BCT 2)	wt% ox	74.53	0.29	13.06	2.19	0.05	0.29	1.29	0.15	3.08	4.99	0.04	0.04		96.70
Exp glass	wt% ox	74.64	0.30	13.18	1.90	0.06	0.29	1.22	0.18	3.00	5.16	0.06	0.00	0.03	99.62
EPMA $n = 162$	*std dev*	*0.33*	*0.02*	*0.14*	*0.09*	*0.01*	*0.03*	*0.04*	*0.02*	*0.08*	*0.09*	*0.02*	*0.00*	*0.01*	*0.42*
Natural glass	wt% ox	77.02	0.18	11.95	1.21	0.08	0.13	0.50	0.09	2.93	5.70	0.05	0.04	0.12	98.22
EPMA $n = 58$	*std dev*	*0.82*	*0.01*	*0.18*	*0.11*	*0.07*	*0.06*	*0.03*	*0.01*	*0.17*	*0.25*	*0.01*	*0.02*	*0.01*	*0.99*

Bulk analysis performed by FUS ICP, ACTLABS Laboratory, Ontario, Canada; Standard deviation (std. dev.) in wt%. Single values normalized to 100 % dry mass

Experimental results

Phase assemblages and proportions

Experimental results are listed in Tables 3 and 4. Most of the experimental temperatures were chosen to reproduce the temperature range determined from thermometry (800–900 °C). Only experiments, with no significant weight loss observed post-run, are listed in Tables 3 and 4 (no volatile loss from the capsule during experiment). The run products of the crystallization experiments were examined by optical microscope and electron microprobe analysis (EMPA). The mineral compositions were used for mass balance calculations to estimate the crystal proportion on the one hand and to check for undetected mineral phases on the other hand. In some cases, the phase compositions could not be determined accurately with microprobe (small phases or intergrowth of several phases) and assumptions on the

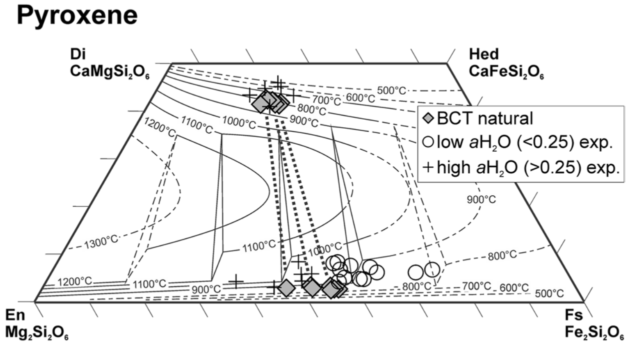

Fig. 3 Ternary En–Fs–Wo plot of Blacktail Creek Tuff pyroxene compositions; filled rhombs represent the compositions of natural Blacktail Creek Tuff pyroxenes. *Crosses* are experimental results with high water activity ($aH_2O > 0.25$) over the full experimental PT range. *Circles* represent experiments containing low amounts of water ($aH_2O < 0.25$). The isotherms are taken from Lindsley (1983)

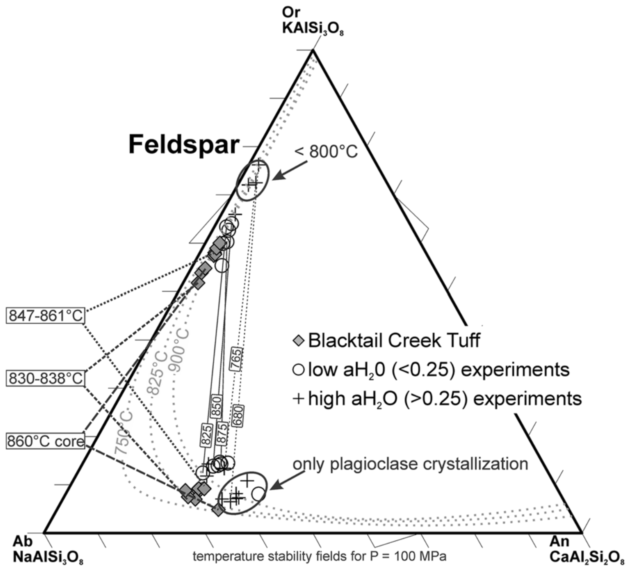

Fig. 4 Ternary Ab–An–Or plot of Blacktail Creek Tuff feldspar compositions. Filled rhombs represent the natural phase composition of Blacktail Creek Tuff plagioclases and sanidines. *Crosses* are experimental results with high water activity ($aH_2O > 0.25$) over the full experimental PT range. *Circles* represent experiments containing low amounts of water ($aH_2O < 0.25$). Isotherms are taken from Fuhrman and Lindsley (1988). Numbers in boxes are temperatures in °C for feldspar pairs

composition of phases were used to estimate phase proportions. Moreover, mass balance calculations were also useful to check for loss of alkalis during microprobe measurement of water-rich glasses.

The experimental products are similar to those described in other experimental studies on phase relationships in rhyolitic systems with typical size of <5 to 40 µm for pyroxenes and feldspars (for typical pictures of run products, see Almeev et al. 2012). In experiments with very low water contents or at nominally anhydrous conditions, the crystal content was often very high (up to >90 %) and the strong undercooling resulted in an intergrowth of different phases, making accurate microprobe analyses of pure phases difficult. In addition, the phase compositions may be far from equilibrium. Such experimental products were not used for interpretations and have been excluded from all plots and tables.

The experimental results were used to establish three phase diagrams (Figs. 8, 9, 10) for the following conditions: fluid-present conditions at 200 MPa (T vs. melt H_2O content, Fig. 8), fluid-absent conditions at 200 MPa (T vs. added H_2O, Fig. 9) and fluid-absent conditions at 900 °C (P vs. added H_2O, Fig. 10). The phase diagram established at fluid-present conditions shows the stability field of phases as a function of the melt water content (which is proportional to aH_2O), following the representation used by Clemens and Wall (1981) and several other studies on rhyolitic systems (e.g., Scaillet et al. 1995; Klimm et al. 2008). Plagioclase is the first tectosilicate phase which crystallizes, followed by sanidine and quartz. In the high temperature—low aH_2O range, pigeonite (in addition to magnetite) is observed as the stable Fe–Mg-bearing phase. The experimental results indicate that augite is stable at lower temperatures, but the coexistence of augite and pigeonite could not be detected in the experimental products. Biotite is observed at lower temperatures and higher aH_2O.

The phase diagram established at fluid-absent conditions and 200 MPa is presented as a function of the added water content in the charge, following the classical diagrams established by Wyllie (1971) and Whitney (1988). Although the two types of representations of phase diagrams (fluid-absent vs. fluid-present) cannot be directly compared, the experimental data obtained at fluid-absent conditions given in Table 3 are in general good agreement with the fluid-present experiments for the stability of tectosilicate phases. In contrast, the stability of the Fe–Mg-bearing phases differs in the fluid-present and fluid-absent experiments. Augite was not observed in fluid-absent experiments over the experimental range of 680–875 °C at 200 MPa, whereas augite was detected in six experiments at fluid-present conditions in the same temperature range (Figs. 8, 9, 10). In the fluid-absent experiments, biotite is present as the Fe–Mg-bearing phase at low temperatures, and the coexistence of pigeonite and biotite was noted in one experiment (850 °C, 2.8 wt% added water). As for fluid-present experiments, pigeonite is the high-temperature Fe–Mg-bearing phase. Possible explanations for this difference between fluid-present and fluid-absent conditions are given in the discussion.

The experiments at 900 °C and 100, 300 and 500 MPa were conducted mainly to check for the effect of pressure on the composition of melts coexisting with tectosilicates. The results in Fig. 10 show that liquidus conditions are

Table 2 Chemical composition of Blacktail Creek Tuff phases and used pairs for temperature calculations

Mineral	*n*	Normative components			Calculation method				
		Usp	Ilm	Mg#	Andersen Ilmat		Ghiorso and Evans (2008)		
					T °C calc	fO_2	T °C calc	fO_2	$aTiO_2$
Ti-magnetite all	*51*	0.42		1.79	854	−13.03	865	−13.09	0.53
Ilmenite all	*21*		0.90	5.26					
Ti-magnetite pair a	*8*	0.41		1.74	875	−12.43	895	−12.15	0.56
Ilmenite pair a	*5*		0.88	5.16					
Ti-magnetite pair b	*5*	0.45		1.99	877	−12.60	889	−12.52	0.55
Ilmenite pair b	*5*		0.90	4.99					
Ti-magnetite pair c	*5*	0.42		1.73	840	−13.39	853	−13.46	0.52
Ilmenite pair c	*5*		0.91	4.70					
					862	−12.86	876	−12.81	0.54

		En	Fs	Wo	Jd/Aeg		Putirka	Quilf		Pigeonite calculated		Augite calculated	
							T °C calc	T °C calc	fO_2	T °C calc	fO_2	T °C calc	fO_2
Pigeonite all	*29*	44.5	52.1	3.4	0.0	47.4	827	892 (47)	−12.58	842	−13.55	926	−11.98
Augite all	*104*	35.0	22.5	41.4	1.1	62.3							
Pigeonite pair a	*3*	48.0	48.5	3.5	0.0	51.2	828	931 (22)	−11.90	841	−13.56	955	−11.50
Augite pair a	*3*	34.0	23.7	41.2	1.2	60.4							
Pigeonite pair b	*1*	48.0	48.5	3.5	0.0	51.0	848	934 (18)	−11.86	862	−13.15	955	−11.50
Augite pair b	*7*	34.5	23.6	40.7	1.1	60.9							
Pigeonite pair c	*3*	43.3	53.9	2.8	0.0	45.9	828	843 (47)	−13.51	860	−13.19	857	−13.25
Augite pair c	*4*	35.1	22.8	40.9	1.1	62.1							
Pigeonite pair d	*5*	44.1	53.1	2.8	0.0	46.7	809	835 (59)	−13.68	825	−13.89	861	−13.17
Augite pair d	*5*	36.2	20.6	42.1	1.2	65.2							
Pigeonite pair e	*2*	47.9	49.1	3.0	0.0	50.8	824	885 (18)	−12.71	836	−13.66	903	−12.39
Augite pair e	*5*	35.2	22.0	41.6	1.2	63.0							
Pigeonite pair f	*5*	44.8	52.6	2.6	0.0	47.4	815	829 (46)	−13.81	839	−13.61	843	−13.53
Augite pair f	*5*	36.0	21.0	41.7	1.2	64.6							
Pigeonite pair g	*5*	52.7	44.3	3.0	0.0	55.8	832	915 (13)	−12.17	861	−13.17	929	−11.94
Augite pair g	*5*	36.9	20.5	41.3	1.3	65.9							
							826	883	−12.8	846	−13.5	904	−12.4

		An	Ab	Or	Cls	Putirka	
						Plag san	Plag liq
Plagioclase all	*58*	24.5	66.5	8.8	0.1	860	866
Sanidine all	*72*	2.7	39.3	55.1	2.9		
Plagioclase a	*6*	24.0	67.0	8.8	0.1	847	865
Sanidine a	*3*	2.9	39.7	54.4	3.0		
Plagioclase b	*2*	25.2	65.6	9.2	0.0	856	867
Sanidine b	*3*	3.0	39.4	54.6	3.0		
Plagioclase c	*6*	24.2	66.6	9.1	0.1	858	866
Sanidine c	*10*	2.6	38.4	55.8	3.2		
Plagioclase d	*4*	25.2	65.6	9.1	0.1	861	867
Sanidine d	*5*	2.7	37.3	56.7	3.3		
Plagioclase e rim	*5*	24.7	68.3	7.0	0.0	838	861
Sanidine e	*5*	2.4	43.8	51.7	2.1		
Plagioclase e core	*5*	30.0	65.1	4.9	0.0	860	861
Sanidine e	*5*	2.4	43.8	51.7	2.1		

Table 2 continued

		An	Ab	Or	Cls	Putirka	
						Plag san	Plag liq
Plagioclase f	*3*	23.1	69.4	7.5	0.0	833	860
Sanidine f	*3*	2.8	45.5	49.2	2.6		
Plagioclase g	*1*	21.9	69.3	8.5	0.3	830	862
Sanidine g	*3*	2.6	42.6	52.1	2.7		
						849	864

Usp Ulvospinell, *Ilm* Ilmenite, *Mg#* Mg number, *En* Enstatite, *Fs* Ferrosilite, *Wo* Wollastonite, *Jd/Aeg* Jadeite/Aegirine, *An* Anorthite, *Ab* Albite, *Or* Sanidine, *Cls* Celsian, *plag san* two-feldspar thermometer and *plag liq* plagioclase–melt thermometer, and values in boxes are average temperatures depending on the method

reached with ~4 wt% H_2O in the melt at 500 MPa, whereas ~1.5 wt% H_2O is necessary at 100 MPa. It can also be noted that titanomagnetite is not present in the experiments at 900 °C which is due to the lower oxygen fugacity prevailing in these experiments conducted in an IHPV (Table 3). From the experiments slightly below the liquidus, it can be noted that the stability of feldspar phases is strongly dependent on pressure. At 500 MPa sanidine is the first occurring phase, whereas plagioclase is the first to occur at 100 MPa. At 300 MPa and ~1.0 wt% H_2O in the melt, the experiments do not allow us to determine the crystallization sequence, and both phases probably start to crystallize within a small temperature interval.

Phase compositions

The compositions of experimental pyroxenes are given in Electronic Supplementary Table 4 and Fig. 3. The composition of augite, obtained experimentally at fluid-present conditions only, ranges from $Fs_{18}Wo_{41}En_{39}$ to $Fs_{26}Wo_{46}En_{31}$, and this compositional range is within that of the natural augites (Fig. 3). The compositions of pigeonite obtained experimentally cover a broader range and vary from $Fs_{34}Wo_3En_{63}$ to $Fs_{69}Wo_9En_{24}$. A systematic effect of temperature is not observed within the investigated range. The high variation in En and Fs components of pigeonite seems to be mainly related to variations in water activity, as already noted by Almeev et al. (2012) for a more Fe-rich high-silica rhyolite. Pigeonite crystallizing at low water activity has higher Fs contents than pigeonite crystallizing at high water activity. However, the natural pigeonites are within the experimentally generated compositional trend (Fig. 3). Pigeonites from our experiments often contain slightly higher Wo than the natural phases (high Wo contents of ~2 %).

The compositions of experimental feldspars are given in Electronic Supplementary Table 4. In addition to Ab, Or and An components, the feldspars contain non-negligible proportions of Cls (Celsian component) which can reach values up to 5 % in sanidine. The Cls component in plagioclase is lower (<1 %). Figure 4 shows the proportions of Ab, An and Or components in experimental and natural phases, where the Cls component is added to the Or component. The An content of plagioclases ranges from 16 to 36 mol % and is similar to the range of natural samples (An_{22}–An_{30}). From Fig. 4, it can be noted that plagioclases from experiments at low water activity have higher Or components than natural plagioclase. However, high Or contents in plagioclase are only observed in run products with high crystallinity that contain two feldspars. In such products, an intergrowth of both feldspar phases is commonly observed, and the measured high Or contents may be related to analytical problems because the composition of individual phases cannot be determined accurately. The Or contents of plagioclases determined in run products of fluid-absent experiments with low crystallinity and containing plagioclase only are systematically low and range from Or_7 to Or_{11}, consistent with natural phases (Or_5–Or_9). The sanidines obtained experimentally cover the natural compositional range. The experiments containing sanidine with high Or contents (Or_{70} and above), which are not observed in the natural sample, were conducted at low temperatures (<800 °C) and at high water activities.

Oxides (titanomagnetite and ilmenite) that crystallized in nearly all experiments are usually too small to obtain accurate EMPA. To get compositional information about oxide compositions, we recalculated the Fe, Ti and Mg concentrations of titanomagnetite and ilmenite by excluding all other elements for normalization. The resulting values were used only to determine ulvöspinel or ilmenite components, but were not used to determine experimental redox conditions (Table 4; Electronic supplement Table 4). The conditions in IHPV experiments are more reducing than in CSPV experiments, which are confirmed by the presence of ilmenite in IHPV run products. In CSPV experiments, oxides are also enriched in Ni, especially in long-duration experiments at temperatures above 800 °C, which is caused by Ni diffusion through the gold capsules from the Ni steel rod of the vessel.

Table 3 Experimental conditions and phase assemblage for Blacktail Creek Tuff

Run	Technique	P (MPa)	T (°C)	Duration (h)	Initial H_2O (wt%)	Melt H_2O (wt%) by difference	Melt H_2O (wt%) FTIR	Melt H_2O (wt%) used for calculation	a H_2O	log (fO_2)	Δ QFM	Phase assemblage and, when possible, phase proportions (mass balance)	R^2	*j* (%)
E01	IHPV	100	900	332	*0.50*$^{++}$	0.6		0.6	0.05	−15.11	−2.65	Gl*(92.1), Pgt*(1.1), Pl*(6.8)	0.15	*7.7*
E02	IHPV	100	900	332	*1.30*$^{++}$	1.1		1.1	0.14	−14.14	−1.68	Gl*(97.5), Pgt*(0.7), Pl*(1.8)	0.07	*2.5*
E03	IHPV	100	900	332	*2.90*$^{++}$	2.2		2.2	0.45	−13.14	−0.68	Gl*(100)	0.08	*0.0*
E04	IHPV	100	900	332	*3.35*$^{++}$	3.3		3.3	0.81	−12.63	−0.17	Gl*(100)	0.10	*0.0*
F05	IHPV	300	900	260	0.50^{+}	1.0		1.0	0.07	−14.66	−2.36	Gl*(79.3), Pgt*(1.2), Pl*(14.1), Sa*(0), Qz*(5.4), Ilm*(0)	0.16	*20.7*
F06	IHPV	300	900	260	2.11^{+}	2.5		2.5	0.29	−13.36	−1.06	Gl*(99.2), Pgt*(0.8),	0.05	*0.8*
F07	IHPV	300	900	260	3.50^{+}	3.6		3.6	0.50	−12.90	−0.60	Gl*(100)	0.15	*0.0*
F08	IHPV	300	900	260	6.49^{+}	6.5		6.5	1.02	−12.28	0.02	Gl*(100)	0.11	*0.0*
F09	IHPV	500	900	226	0.50^{+}	2.0		2.0	0.16	−13.75	−1.60	Gl*(86), Pgt*(0.1), Pl(9.2), Sa*(0), Qz(4.6), Mag*(0), Ilm*(0)	0.18	*14.0*
F10	IHPV	500	900	226	4.00^{+}	4.7		4.4	0.49	−12.77	−0.62	Gl*(98.2), Pgt(1), Sa*(0.8)	0.01	*1.8*
F11	IHPV	500	900	226	5.29^{+}	5.8		5.6	0.65	−12.52	−0.37	Gl*(100)	0.11	*0.0*
F12	IHPV	500	900	226	9.27^{+}	8.7		8.5	1.01	−12.14	0.01	Gl*(100)	0.12	*0.0*
A09	CSPV	200	875	888	*0.00*	0.9		0.9	0.07	−14.20	−1.37	Gl*(77.9), Pgt*(1.6), Pl*(16.4), Sa*(0), Qz(4), Mag*(0.2)	0.11	*22.1*
M06	CSPV	200	875	672	*0.80*$^{++}$	1.0	1.4	1.3	0.12	−13.68	−0.85	Gl*(85.8), Pgt*(1.6), Pl*(9.9), Sa*(0), Qz(2.4), Mag*(0.4)	0.20	*14.2*
M07	CSPV	200	875	672	*1.30*$^{++}$	1.7	1.4	1.5	0.16	−13.44	−0.61	Gl*(88.3), Pgt*(1), Pl*(10), Qz(0.1), Mag(0.6)	0.06	*11.7*
M08	CSPV	200	875	672	*2.90*$^{++}$	2.4	3.0	3.0	0.48	−12.47	0.36	Gl*(99.4), Pgt*(0.3), Mag*(0.3)	0.01	*0.6*
A12	CSPV	200	875	888	*5.00*$^{++}$	5.2		5.1	0.93	−11.90	0.93	Gl*(99.1), Mag*(0.9)	0.09	*0.9*
A13x	CSPV	200	850	864	*0.00*	0.7		0.7	0.04	−15.04	−1.74	Gl*(80.4), Pgt*(1.8), Pl(14.2), Sa*(0), Qz(3.5), Mag*(0.1)	0.18	*19.6*
A14x	CSPV	200	850	864	*0.80*$^{++}$	1.3		1.3	0.13	−14.10	−0.80	Gl*(82.3), Pgt*(1.4), Pl*(12.1), Sa*(0), Qz(3.7), Mag*(0.4)	0.17	*17.7*
A15x	CSPV	200	850	864	*1.30*$^{++}$	1.6		1.6	0.18	−13.80	−0.50	Gl*(86.5), Pgt*(1.5), Pl*(10.7), Sa*(0), Qz*(1.1), Mag*(0.3)	0.20	*13.5*
A16x	CSPV	200	850	864	*2.90*$^{++}$	2.2		2.5	0.36	−13.18	0.12	Gl*(94.7), Pgt*(0.3), Bt*(0.8), Pl*(3.8), Mag*(0.5)	0.03	*5.2*
A16	CSPV	200	850	912	5.26^{+}	5.4		5.4	1.01	−12.29	1.01	Gl*(99), Mag*(1)	0.06	*1.0*
A18x	CSPV	200	825	1368	*0.80*$^{++}$	1.9		1.9	0.24	−14.04	−0.25	Gl*(84.5), Bt*(2.1), Pl*(9.6), Sa*(0), Qz(2.8), Mag*(0.9)	0.23	*15.5*
A18	CSPV	200	825	888	*1.30*$^{++}$	1.5		1.5	0.15	−14.43	−0.64	Gl*(82.3), Pgt*(1.6), Pl*(12.5), Sa*(0), Qz*(3.2), Mag*(0.1), Ilm*(0.1)	0.01	*17.7*
A20x	CSPV	200	825	1368	*2.90*$^{++}$	2.4		2.4	0.33	−13.75	0.04	Gl*(89.9), Pl*(8.9), Mag*(1.3)	0.13	*10.1*
A20	CSPV	200	825	888	*5.00*$^{++}$	4.7		4.7	0.85	−12.93	0.86	Gl*(99), Mag*(1)	0.12	*1.0*

Table 3 continued

Run	Technique	P (MPa)	T (°C)	Duration (h)	Initial H_2O (wt%)	Melt H_2O (wt%) by difference	Melt H_2O (wt%) FTIR	Melt H_2O (wt%) used for calculation	a H_2O	log (fO_2)	Δ QFM	Phase assemblage and, when possible, phase proportions (mass balance)	R^2	*j* (%)
A22	CSPV	200	800	936	*1.30*$^{++}$	2.1		2.1	0.27	−14.43	−0.12	Gl*(53.5), Bt*(1.8), Pl(16.6), Sa*(15.3), Qz*(11.9), Mag*(0.9)	0.12	*46.5*
A23	CSPV	200	800	936	*2.90*$^{++}$	2.7		2.7	0.40	−14.10	0.21	Gl*(73.3), Bt*(2.1), Pl*(14.5), Sa*(3.3), Qz*(5.8), Mag*(1)	0.04	*26.7*
A24	CSPV	200	800	936	5.22^{+}	5.3		5.3	1.01	−13.30	1.01	Gl*(98.8), Mag*(1.2)	0.14	*1.2*
JI 21	CSPV	200	700	408	11.70^{+}	6.4	6.3	6.4	1.17	−15.49	1.14	Gl*(97.4), Bt*(1.8), Mag*(0.9)	0.04	*2.6*
JI 12	CSPV	200	680	408	10.80^{+}	5.9	4.6	5.5	1.00	−16.16	0.99	Gl*(91.7), Bt(1.4), Pl*(0), Sa*(5.9), Mag(1)	0.08	*8.3*
M14	CSPV + CO2	200	875	672	*0.66*$^{++}$	1.1	1.3	1.2	0.11	−13.73	−0.90	Gl*(59.1), Pgt*(1.9), Pl(11.8), Sa*(14.8), Qz(11.7), Mag*(0.7), Ilm*(0)	0.03	*40.9*
M15	CSPV + CO2	200	875	672	*1.18*$^{++}$	1.8	1.4	1.6	0.18	−13.33	−0.50	Gl*(71.4), Pgt*(1.6), Pl*(10.6), Sa*(8.2), Qz(7.9), Mag(0.4), Ilm*(0)	0.09	*28.6*
M16	CSPV + CO2	200	875	672	*2.34*$^{++}$	2.4	2.6	2.5	0.37	−12.69	0.14	Gl*(92.4), Pgt*(1.7), Pl*(5.4), Mag*(0.5)	0.18	*7.6*
M11	CSPV + CO2	200	850	672	*1.18*$^{++}$	1.0	1.4	1.2	0.11	−14.23	−0.93	Gl*(64.4), Pgt*(0.7), Pl*(14), Sa*(10), Qz(9.8), Mag*(1.1)	0.15	*35.6*
M12	CSPV + CO2	200	850	672	*2.31*$^{++}$	2.0	2.5	2.3	0.32	−13.30	0.00	Gl*(90), Aug*(0.9), Pl*(8.6), Mag*(0.5)	0.18	*10.0*
JI 63	CSPV + CO2	200	815	336	3.90^{+}	3.2	3.7	3.5	0.56	−13.49	0.51	Gl*(99.3), Aug*(0.1), Mag*(0.6)	0.06	*0.7*
JII 44	CSPV + CO2	200	815	672	4.65^{+}	3.9		3.7	0.63	−13.40	0.60	Gl*(98.5), Mag*(1.3)	0.04	*1.5*
JI 53	CSPV + CO2	200	790	336	3.50^{+}	3.3	3.8	3.6	0.59	−13.98	0.54	Gl*(90.6), Aug*(0.5), Bt(2), Pl*(6.4), Mag*(0.6)	0.09	*9.2*
JII 34	CSPV + CO2	200	790	672	4.50^{+}	3.9		3.9	0.68	−13.86	0.66	Gl*(95.2), Aug*(0), Pl(3.7), Mag*(1.1)	0.08	*4.8*
JII 54	CSPV + CO2	200	765	672	4.65^{+}	3.3		3.3	0.53	−14.63	0.44	Gl*(89.4), Aug*(0.7), Pl*(6), Sa*(2.6), Mag*(1.3)	0.01	*10.6*
JI 43	CSPV + CO2	200	765	336	4.31^{+}	3.5		3.5	0.57	−14.56	0.51	Gl*(89), Aug*(0.4), Bt(1.6), Pl*(8.4), Sa*(0), Mag*(0.6)	0.07	*10.8*

++Pre-hydrated glass; +H2O added to glass; * Phases with successful microprobe measurements; CSPV experiments at intrinsic conditions (~NNO), IHPV experiments with controlled oxygen fugacity at ~QFM, both given for water-saturated experimental conditions; mineral abbreviations as before and *Gl* matrix glass, *Mag* Titanomagnetite; *Ilm* ilmenite, *Bt* biotite; R^2 error of mass balance calculations; *j*(%) mineral proportion (vol%)

Experimentally grown biotite is very small, and the minerals also often contain inclusions of oxides. It is therefore difficult to obtain accurate analyses with EMPA. The analytical results of phases which could be analyzed are given in Table 3 and Electronic supplement Table 4, but it is emphasized that the compositions need to be interpreted with caution. However, it can be noted that the Ti concentration is relatively high (~4.00 wt%) as well as the Mg# ranging from 0.39–0.83. The Mg# of the natural biotite which could be detected is at the low end of the range (0.38), which could indicate that the oxygen fugacity in the natural system is lower than that in our experiments. However, only one small biotite grain, with resorption texture, was found in the thin section of the natural sample, and this observation needs to be treated with caution.

The composition of experimental glasses is given in Table 4 and Electronic supplement Table 4 and plotted in selected binary diagrams in Fig. 5. Our experimentally generated glasses follow the natural compositional evolution trend with ongoing enrichment in SiO_2. The experimental glass compositions that best reproduce the natural glass matrix are obtained at low water contents. The elements incorporated in tectosilicate oxides such as Al, Ca, Na, K plot within the natural matrix glass field. Mafic elements (Fe, Ti) show slight shifts when compared to the natural glasses (see Fig. 5). Matrix glass compositions are best reproduced at low water contents (<2wt% H_2O) and temperatures >800 °C. The composition of some glass inclusions, especially the K_2O-rich inclusions in augite, could not be reproduced in our experiments.

Discussion

Attainment of equilibrium

Reaching equilibrium in crystallization experiments at low water activities and in SiO_2–rich starting compositions is challenging. The low diffusivities of network-forming elements (Si, Al) control the kinetics of crystallization. A detailed discussion on the conditions necessary to attain near-equilibrium conditions at fluid-present conditions with the same type of starting composition (high-silica rhyolite of Snake River Plain) is given in Almeev et al. (2012) and is not repeated here. In particular, compositional equilibrium between all phases and equilibrium in terms of melt/crystal proportions is very difficult to achieve in experimental runs, especially in highly crystalline products and for rhyolitic systems (e.g., Pichavant et al. 2007). Taking these limitations into account, Almeev et al. (2012) demonstrated that near-equilibrium conditions can be reached in experimental products with crystal fractions below 30 vol% within the run durations and the experimental temperatures applied in this study.

Experiments at fluid-absent conditions were not performed by Almeev et al. (2012), and the difference between the two phase diagrams determined at fluid-present and fluid-absent conditions may be related to kinetic problems. Problems related to nucleation are probably similar in both approaches. The best method to minimize strong undercooling and to enhance nucleation throughout the whole charge is to use powder as starting material because nucleation preferentially occurs at the boundary between the initial glass grains as demonstrated by Pichavant (1987) at fluid-present conditions and by Becker et al. (1998) at fluid-absent conditions. The best evidence indicating that nucleation and growth should not be a severe problem at the experimental conditions applied in this study (long run durations) is the observation of experimental products with very high crystallinity (up to ~90 % crystals) when the water content and/or the temperature was low. In case of significant problems related to crystal growth, such high crystallinity would not be observed.

Assuming that nucleation and growth in general is not a problem in both types of experiments (the starting material was glass powder), problems specifically related to crystal growth or to the nucleation of augite may have occurred at fluid-absent conditions. The crystallization process in a pre-hydrated glass (fluid-absent) and in a dry glass in the presence of a H_2O–CO_2-bearing fluid is not identical, and some phases may nucleate preferentially in the presence of a fluid. The results in this study would indicate that the nucleation of augite is inhibited in fluid-absent experiments and/or that the nucleation of biotite is inhibited in fluid-present conditions. Although biotite often forms very tiny crystals in experimental products of granitic systems, nucleation problems in fluid-present experiments are not expected, taking into account previous observations indicating that biotite grows preferentially from the fluid (Puziewicz and Johannes 1988). The crystals of augite in the fluid-present experiments have idiomorphic shapes and do not show resorption textures, excluding a fast growth in the first stages of the experiment and subsequent dissolution. Thus, there is no evidence for disequilibrium in the fluid-present experiments. In addition, augite is observed in preliminary experiments conducted with a slightly different bulk composition (slightly more evolved with less Ca than the composition Blacktail Creek Tuff, Bolte et al. unpublished results). The experimental procedure was similar (with pre-hydrated glasses), and for this composition, the approach using fluid-absent conditions does not seem to be critical for the nucleation of augite. Thus, we conclude that the different mafic mineral assemblage in fluid-absent and fluid-present experiments is not primarily related to kinetic problems.

Phase diagrams

Two significant differences between the two types of experiments, fluid-present and fluid-absent, are observable: (1) There is no stability field for augite in fluid-absent experiments (H_2O only) and (2) the stability field for biotite shifts toward lower temperatures in fluid-present experiments when compared to the fluid-absent experiments (Figs. 8, 9). This difference is surprising but experiments with the two approaches (fluid-present and fluid-absent) using the same bulk composition have not been done previously. Assuming that the differences are not due to kinetic problems (see above), different reasons may cause this discrepancy. (1) The presence of CO_2 may change the melt structure and affect the crystallizing phases. This is not expected to be the case because the solubility of CO_2 is low in rhyolitic melts and because C is incorporated as molecular CO_2 (e.g., Tamic et al. 2001; Fogel and Rutherford 1990). (2) The water activity is different in the fluid-absent and fluid-present experiments. Using a H_2O–CO_2-bearing fluid, the water activity or melt water content is controlled by the composition of the coexisting fluid. In contrast, in fluid-absent experiments, the water content of the melt is controlled by the amount of crystals present in the charge. This difference can have a significant effect on the phase assemblage because the evolution of water activity with increasing crystallinity differs if systems crystallize along a fluid-present or a fluid-absent path. For example, following the phase diagram in Fig. 8, and assuming a temperature of 800 °C in a H_2O–CO_2-bearing fluid-present system, the crystallinity can vary from nearly 100 % crystals, if the water content of the melt is ~2 wt%, to nearly 0 % crystals (liquidus) if the melt water content is ~4 wt%. A progressive evolution of crystallinity with the melt water content (or water activity) is expected over this interval (4–2 wt% H_2O in the melt). In a fluid-absent system at 800 °C, crystallization is expected to start at the same melt water content of ~4 wt% H_2O (Fig. 9), but the crystallinity increases at nearly constant melt water content as a result of decreasing added water contents. For example, in case of an eutectic system, a crystal content of ~50 % would be reached with 2 wt% water added. At this value of 2 wt% added H_2O, the minimum amount of water which can be incorporated into silicate melts is reached (~3 wt% at 200 MPa and 800 °C; Holtz et al. 2001). Thus, even if <2 wt% water is added to the system, the melt water content remains at ~3 wt% H_2O and the water activity will remain constant in the high crystallinity range. Consequently, in the crystallization interval investigated in the phase diagrams in this study, with most experiments containing 30 % crystals or less, the water activity should be higher in fluid-present conditions at the same crystal content and same temperature.

The smaller stability field of biotite at slightly higher water activities in fluid-present conditions may be surprising. However, phase relationships established for several rhyolitic or granitic compositions have demonstrated that the crystallization temperature of biotite is not clearly dependent on water activity, but rather on temperature or other compositional parameters (e.g., Naney 1983; Scaillet et al. 1995; Dall'Agnol et al. 1999; Klimm et al. 2003). On the other hand, water activity is known to affect strongly the crystallization temperature of plagioclase (e.g., Scaillet et al. 1995; Dall'Agnol et al. 1999; Klimm et al. 2003). Thus, at higher water activity, a mafic Ca-bearing phase such as augite may crystallize before the crystallization of plagioclase, which is indeed observed in the fluid-absent phase diagram at 800 °C (Fig. 8).

Magma storage conditions from mineral composition and phase equilibria

Temperature

Our 200 MPa experiments at fluid-present conditions indicate that all natural phases (Aug, Pgt, Ilm, Ti-Mag, Pl, Sa and Qz) can only coexist in a restricted field. Assuming that biotite is not stable in the natural assemblage, the temperature of magma storage conditions is most probably above 750–800 °C. Experiments containing higher water contents (>3 wt% H_2O) at low experimental temperatures (<800 °C) do not reproduce the natural assemblage. The fluid-present phase diagram (Fig. 8) indicates that pigeonite and augite stability fields may overlap over a temperature range of 800–875 °C, depending on the melt water content (1–2.5 wt% H_2O, respectively). Considering that the low-temperature boundary of the stability field of pigeonite is similar at fluid-present and fluid-absent conditions, this temperature can be considered as minimum value.

The temperature range 800–875 °C is within that constrained by the Plag-liquid and two-feldspar thermometers indicating temperatures in a range 830–870 °C with average temperatures of 849 and 864 °C, respectively (Table 2). These temperatures are also in agreement with the data from zircon and apatite solubility models at ~860 °C. The ilm-magnetite thermometer (Andersen et al. 1993; Lindsley 1983; Stormer 1983; Ghiorso and Evans 2008) predicts temperatures ~15 °C higher (876 °C). Thus, taken as a whole, a pre-eruptive temperature of ~860 ± 15 °C is probably realistic. The comparison with the two-pyroxene temperatures is difficult. Temperature calculations with natural Aug–Pgt pairs yield a large temperature variation and large errors, which indicates disequilibrium between the two phases, possibly related to different sources for the pyroxenes (e.g., different magma batches, see below).

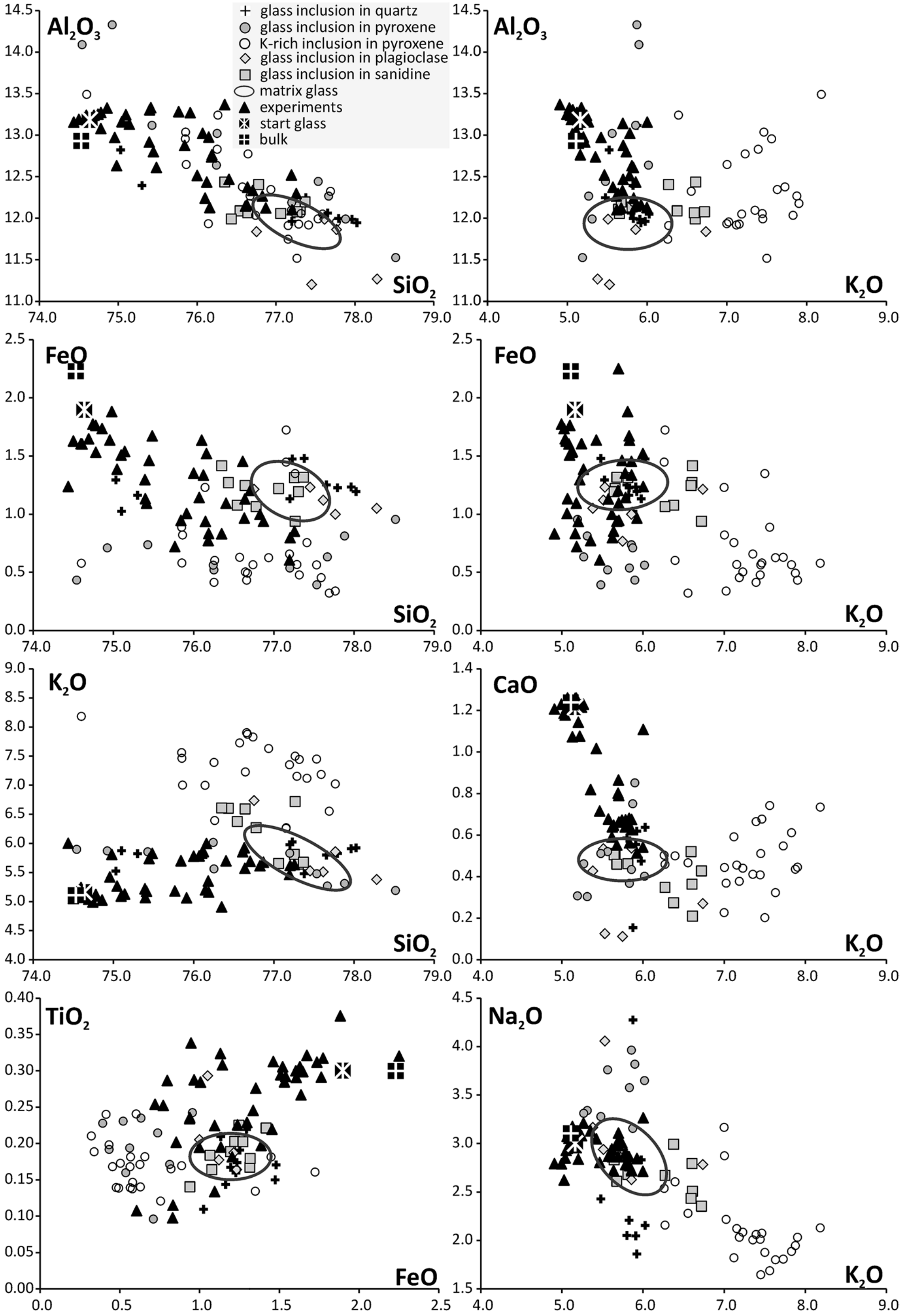

Fig. 5 Binary plots displaying Blacktail Creek Tuff bulk composition, matrix glass and experimental glass (wt% oxides normalized to 100 %). Blacktail Creek Tuff melt inclusions are grouped by host mineral. Note the changing oxides on the *x*-axis and the relatively small variations between bulk composition and starting glass

Melt water content

Assuming temperatures of ~860 ± 15 °C and a pressure of 200 MPa, the constraints given by the fluid-present phase relationships (coexistence of Aug and Pgt) indicate that the water content of the melt is above 2 wt% H_2O. At low water contents ($aH_2O < 0.25$), the Or content in experimental sanidine and the En content in experimental pigeonite are higher than in the natural minerals (Figs. 3, 4). The composition of mineral phases is best reproduced at water activities (aH_2O) ~0.25 (Figs. 3, 4) which correspond to a water content of ~1.5–2 wt% H_2O. Assuming a water content of 1.5 wt% and a temperature in the range 850–870, the crystal content is expected to be higher than that observed in natural samples (16 vol%). Thus, a water content of ~2 wt% is probably realistic and would reproduce the phase assemblage, the phase proportions and the phase compositions. Using the Ti-in-quartz thermobarometer and

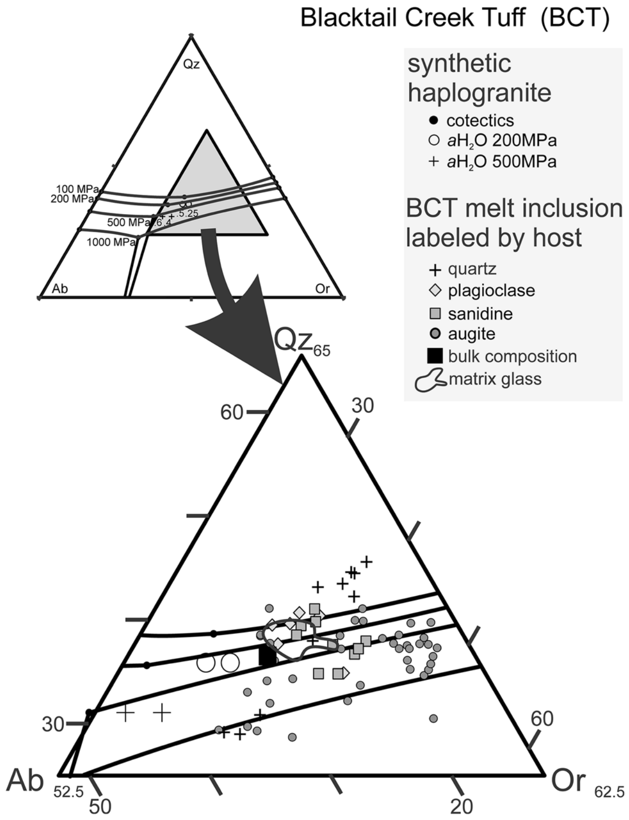

Fig. 6 Ternary Qz–Ab–Or plot of Blacktail Creek Tuff glasses in relationship to cotectic lines in the haplogranitic Qz–Ab–Or system (Holtz et al. 1992). Different glass compositions are designated by source or host mineral as given in the key

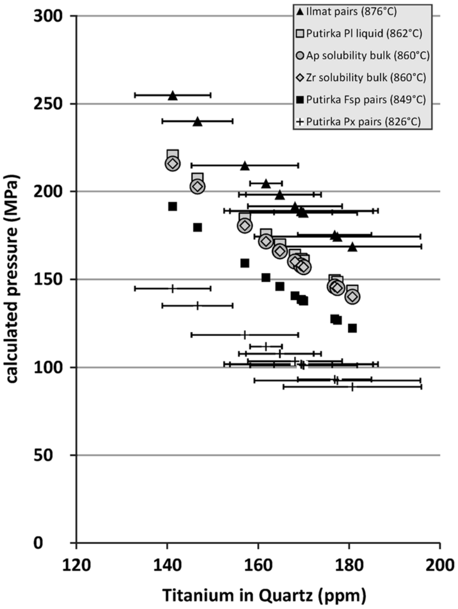

Fig. 7 Binary plot of measured titanium contents [ppm] in Blacktail Creek Tuff quartz phenocrysts, including calculated pressures after Huang and Audetat (2012). Titanium contents are measured by microprobe (EMPA). Temperatures used for calculations are taken from the various geothermometers given in the key. The titanium activity ($a\text{TiO}_2$) in the system is calculated after Ghiorso and Evans (2008) and fixed at $a\text{TiO}_2 = 0.54$ (see Table 2). The diagram illustrates the possible pressure range applying all calculated temperatures. Results of titanium-in-quartz measurements are given in Electronic Supplement Table 6

applying a temperature of 850–870 °C, the pressure can be estimated to be in the range 130–240 MPa, respectively.

Magma storage conditions from the composition of cotectic melts

The experimental results can be used to calibrate the compositions of melts coexisting with quartz and feldspar(s) in natural Blacktail Creek Tuff magmas. By analogy to the haplogranite system, such melts are considered to have cotectic or eutectic compositions, although this is not absolutely correct considering that non-negligible amounts of An- and Fe-bearing components are present in the natural systems. The results of experiments generating all three tectosilicate phases (quartz, sanidine and plagioclase) were used to project eutectic compositions on the Q–Ab–Or plane (Figs. 11, 12). Fluid-absent as well as fluid-present experimental results have been used. It is emphasized that all three experimental glasses synthesized at 200 MPa, under fluid-absent conditions and nearly the same water activity have nearly the same Qz–Ab–Or proportions. Temperature variations of 50 °C have only little effect (see Fig. 11). We are able to localize the eutectic point for Blacktail Creek Tuff magma composition for 200 MPa and $a(H_2O)$ ~0.1 at Qz $_{40}$ Ab $_{23}$ Or $_{37}$, for 300 MPa and $a(H_2O)$ ~0.1 at Qz $_{36}$ Ab $_{27}$ Or $_{37}$ and for 500 MPa and $a(H_2O)$ ~0.2 at Qz $_{33}$ Ab $_{30}$ Or$_{37.}$

Compared with the eutectic (or minimum) compositions of the haplogranitic system, the typical shift of the eutectic point with decreasing water activity toward the Qz–Or sideline and the typical shift with increasing pressure toward the Ab–Or sideline, which is expected from the investigations in the haplogranite system (e.g., Tuttle and Bowen 1958; Holtz et al. 1992), is confirmed. These observations are independent from the experimental approach (fluid-present or fluid-absent), which demonstrates that the presence of CO_2 is not responsible for the changes in phase relationships. The presence of An also causes a general shift of eutectic compositions toward the Qz–Or sideline as shown experimentally at 100 MPa (James and Hamilton 1969) and proposed by Blundy and Cashman (2001). Our experimental glasses with low water contents reach normative An contents in the range of $An_{2.2–3.3}$. Thus, the high Or contents of the eutectic compositions of the experimental glasses are most probably the result of the low water activity and the presence of An in the bulk compositions.

Table 4 Experimental runs and phase endmembers for Blacktail Creek Tuff

Run	Melt H_2O	Aug	Pgt	Pl	Sa	Mag	Ilm	Bt	Gl
E01	0.6		En(41)Fs(52.1) Wo(6.9)	An(27)Ab(58.3)Or(14.5) Cls(0.3)					Qz(33)Or(34.5)Ab(24.7)An(4)
E02	1.1		En(46.6)Fs(47.4) Wo(6)	An(35.9)Ab(56.1)Or(7.9) Cls(0.2)					Qz(32.1)Or(32.1)Ab(26.3)An(5.5)
E03	2.2								Qz(32.8)Or(30.1)Ab(26)An(6.6)
E04	3.3								Qz(32.2)Or(31)Ab(26.1)An(6.6)
F05	1.0		En(27.5)Fs(66.2) Wo(6.3)	An(19.3)Ab(57.3) Or(23.4)Cls(0)	An(5.8)Ab(39.6) Or(53.9)Cls(0.7)		X Ilm(0.9)		Qz(33.3)Or(34.3)Ab(24.3)An(3)
F06	2.5		En(48.5)Fs(45.6) Wo(5.9)						Qz(33)Or(30)Ab(25.8)An(6.6)
F07	3.6								Qz(33.7)Or(29.9)Ab(24.8)An(6.5)
F08	6.5								Qz(33.7)Or(29.6)Ab(24.8)An(6.9)
F09	2.0		En(24.2)Fs(68.9) Wo(6.8)	Pl[a]	An(5.4)Ab(39.2) Or(54.8)Cls(0.6)	X Usp(0.7)	X Ilm(0.9)		Qz(30.1)Or(33.7)Ab(26.3)An(3.8)
F10	4.4		Pig[a]		An(12.9)Ab(32.8) Or(53.2)Cls(1)				Qz(34)Or(30.1)Ab(25.2)An(6.4)
F11	5.6								Qz(34.5)Or(29.8)Ab(24.1)An(6.4)
F12	8.5								Qz(34.7)Or(29.2)Ab(24.2)An(6.6)
A09	0.9		En(40.7)Fs(50.9) Wo(8.4)	An(22.5)Ab(58.2) Or(19.3)Cls(0)	An(5.4)Ab(39.1) Or(54.7)Cls(0.8)	X Usp(0.3)			Qz(35.1)Or(35.4)Ab(23)An(2.4)
M06	1.3		En(41)Fs(53.8) Wo(5.2)	An(25.4)Ab(59.9) Or(14.7)Cls(0)	An(3.9)Ab(35.8) Or(60.3)Cls(0)	X Usp(0.5)			Qz(35.4)Or(34.2)Ab(23.5)An(3.3)
M07	1.5		En(42.5)Fs(53.2) Wo(4.4)	An(25.8)Ab(59.9) Or(14.3)Cls(0)		Mt[a]			Qz(35.8)Or(32.9)Ab(24.3)An(4.1)
M08	3.0		En(54.8)Fs(42) Wo(3.1)			X Usp(0.4)			Qz(33.2)Or(30.3)Ab(25.7)An(6.5)
A12	5.1					X Usp(0.2)			Qz(29.6)Or(30.2)Ab(25.9)An(5.5)
A13x	0.7		En(34.6)Fs(59.2) Wo(6.3)	Pl[a]	An(4.2)Ab(40.3) Or(54.8)Cls(0.6)	X Usp(0.5)			Qz(35.3)Or(34.5)Ab(23.3)An(2.6)
A14x	1.3		En(38.4)Fs(56.7) Wo(4.9)	An(20.6)Ab(59.4) Or(20.1)Cls(0)	An(3.1)Ab(36.3) Or(58.8)Cls(1.8)	X Usp(0.5)			Qz(34.1)Or(35.1)Ab(24.7)An(2.8)
A15x	1.6		En(37.7)Fs(57.5) Wo(4.9)	An(20.6)Ab(62.4)Or(17) Cls(0)	An(3.3)Ab(35.1) Or(59.9)Cls(1.8)	X Usp(0.5)			Qz(35.2)Or(33.4)Ab(24.6)An(3.6)
A16x	2.5		En(49.1)Fs(46.4) Wo(4.5)	An(32.6)Ab(60.1)Or(7.3) Cls(0)		X Usp(0.3)		#Mg(0.6)Si/ AlIV(2.7)	Qz(33.9)Or(31.4)Ab(25.2)An(5.7)
A16	5.4					X Usp(0.3)			Qz(34.5)Or(30.6)Ab(25)An(6.8)
A18x	1.9			An(23.3)Ab(64.2) Or(12.5)Cls(0)	An(2.3)Ab(34.4) Or(62.3)Cls(1.1)	X Usp(0.1)		#Mg(0.8)Si/ AlIV(2.5)	Qz(34.6)Or(33.5)Ab(26.5)An(2.9)
A18	1.5		En(35.3)Fs(57.4) Wo(7.3)	An(24.1)Ab(59.1) Or(16.3)Cls(0.5)	An(5.2)Ab(35.1) Or(55.9)Cls(3.8)	X Usp(0.4)	X Ilm(0.9)		Qz(35.1)Or(34.6)Ab(23)An(3.8)

Table 4 continued

Run	Melt H_2O	Aug	Pgt	Pl	Sa	Mag	Ilm	Bt	Gl
A20x	2.4			An(29.6)Ab(63.4)Or(7) Cls(0)		X Usp(0.6)		Bt[a]	Qz(36.4)Or(33.3)Ab(24.4)An(3.5)
A20	4.7					X Usp(0.3)			Qz(34.9)Or(30)Ab(25)An(6.9)
A22	2.1			Pl[a]	An(2.6)Ab(31.5) Or(65.2)Cls(0.7)	X Usp(0.2)		#Mg(0.6)Si/ AlIV(2.7)	Qz(35.9)Or(33.2)Ab(24.9)An(3.3)
A23	2.7			An(21.9)Ab(59.1) Or(17.7)Cls(1.3)	An(1.7)Ab(26.4) Or(67)Cls(4.9)	X Usp(0.2)		#Mg(0.6)Si/ AlIV(2.7)	Qz(35.8)Or(32.1)Ab(23.1)An(2.8)
A24	5.3					X Usp(0.1)			Qz(33.4)Or(28.4)Ab(24.7)An(5.8)
JI 21	6.4					X Usp(0.2)		#Mg(0.4)Si/ AlIV(2.7)	Qz(33)Or(28)Ab(23.9)An(5.9)
JI 12	5.5			An(31.4)Ab(62.1)Or(6.5) Cls(0)	An(1.8)Ab(22) Or(72.8)Cls(3.4)	Mt[a]			Qz(34.1)Or(25.2)Ab(26.4)An(5.3)
M14	1.2		En(38.7)Fs(53.6) Wo(7.7)	Pl[a]	An(3.3)Ab(36.8) Or(58.2)Cls(1.7)	X Usp(0.5)	X Ilm(0.9)		Qz(35.4)Or(34.2)Ab(23.5)An(3.3)
M15	1.6		En(41.5)Fs(50.3) Wo(8.2)	An(25.3)Ab(60.6) Or(13.6)Cls(0.4)	An(3)Ab(34.3) Or(59.3)Cls(3.4)	Mt[a]	X Ilm(0.9)		Qz(33.5)Or(33.9)Ab(25.4)An(3)
M16	2.5		En(47.7)Fs(43.8) Wo(8.5)	An(32.4)Ab(56.8) Or(10.3)Cls(0.5)		X Usp(0.4)			Qz(34.1)Or(33.7)Ab(25.5)An(3.8)
M11	1.2		En(61.2)Fs(34.5) Wo(4.4)	An(24.5)Ab(61.6) Or(13.4)Cls(0.5)	An(2.9)Ab(33.1) Or(61.6)Cls(2.4)	X Usp(0.2)			Qz(35.6)Or(35)Ab(24.1)An(2.2)
M12	2.3	En(39.2)Fs(17.5) Wo(43.3)		An(32.2)Ab(60.7)Or(7.1) Cls(0)		X Usp(0.2)			Qz(35.1)Or(35)Ab(23.4)An(2.8)
JI 63	3.5	En(36.8)Fs(22.4) Wo(40.9)				X Usp(0.3)			Qz(31.7)Or(31.3)Ab(27.4)An(6)
JII 44	3.7					X Usp(0.1)			Qz(34.6)Or(30.6)Ab(25.7)An(6.6)
JI 53	3.6	En(31.3)Fs(25.6) Wo(43.1)		An(24.4)Ab(63.8) Or(11.2)Cls(0.6)		X Usp(0.3)		Bt[a]	Qz(34)Or(33.9)Ab(25.4)An(3.8)
JII 34	3.9	En(35.8)Fs(19.6) Wo(44.6)		Pl[a]		X Usp(0.2)			Qz(36.1)Or(30.7)Ab(24)An(6.3)
JII 54	3.3	En(32.8)Fs(21.4) Wo(45.8)		An(26.8)Ab(59.8) Or(12.8)Cls(0.6)	An(3.2)Ab(24.3) Or(68.5)Cls(4)	X Usp(0.4)			Qz(36.6)Or(31.5)Ab(25.1)An(4.5)
JI 43	3.5	En(32.6)Fs(22.3) Wo(45)		An(23.4)Ab(62.3) Or(13.5)Cls(0.8)	An(2)Ab(25.9) Or(67.4)Cls(4.6)	X Usp(0.2)		Bt[a]	Qz(34.9)Or(33.9)Ab(24.4)An(4)

[a] Detected phases without microprobe measurements and phase calculations

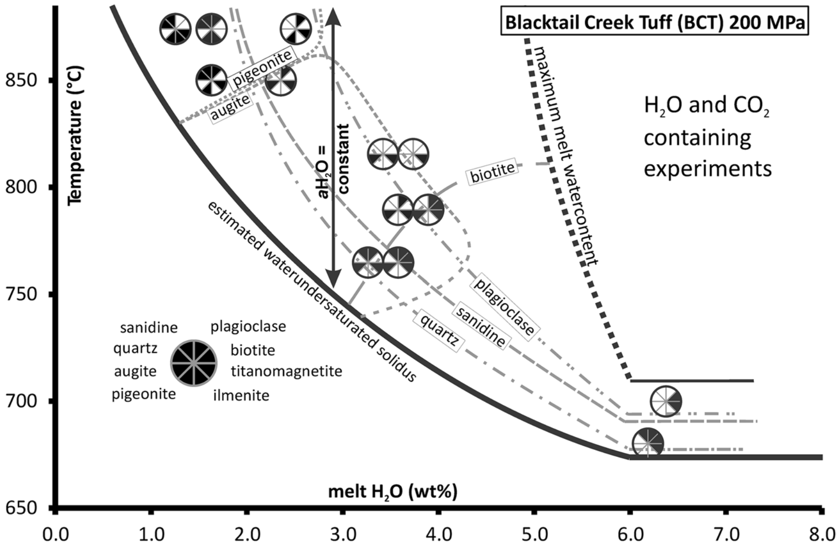

Fig. 8 Phase relations determined for the composition Blacktail Creek Tuff at 200 MPa as a function of temperature and water content in the melt (wt% H_2O) at fluid-present conditions (CO_2 oversaturated). The experimental data are given in Table 3 and Electronic Supplement Table 4. *Solid lines* define stability fields as labeled. The water-saturated liquidus is estimated from the synthetic Qz–Ab–Or system. The *black arrow* illustrates crystallization at constant water activity (aH_2O) and varying crystal content

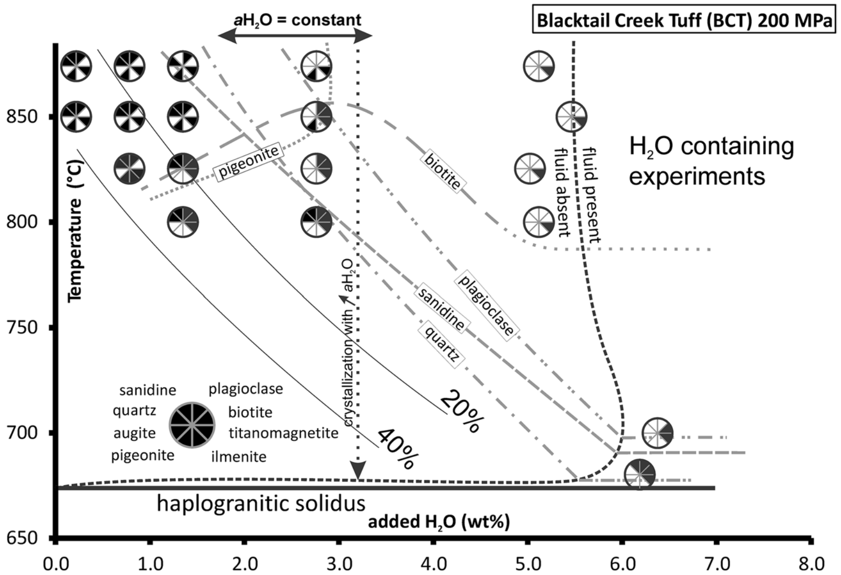

Fig. 9 Phase relations determined for the composition Blacktail Creek Tuff at 200 MPa as a function of temperature and added water content in the system (wt% H_2O) at fluid-absent conditions. The experimental data are provided in Table 3 and Electronic Supplement Table 4. *Solid lines* define stability fields as labeled. *Thin lines* show the degree of crystallization (%) determined by mass balance calculations as labeled. The water-saturated liquidus is estimated from the synthetic Qz–Ab–Or system. The *black arrow* illustrates crystallization at constant water activity (aH_2O) and varying crystal content; the *dashed arrow* shows a crystallization path with increasing aH_2O

The average normative An content of natural Blacktail Creek Tuff matrix glasses is $An_{2.1}$, and the experimental results can be applied to constrain the pressure and water activity prevailing prior to eruption. The Qz–Ab–Or proportions of the natural matrix glasses constrain the pressure in a range between 200 and 300 MPa and melt water contents in the range 3–1 wt% H_2O (see Fig. 12). These conditions overlap with those predicted from phase compositions and geobarometers.

Glass inclusions and pyroxene compositions: possible implications for magmatic processes

The strong compositional variation of glass inclusions, with obviously different populations, deserves special attention. It is emphasized that interpretations need to be conducted with caution since glass inclusions were not re-homogenized. Possible compositional variation may have occurred during cooling as a result of partial crystallization. In

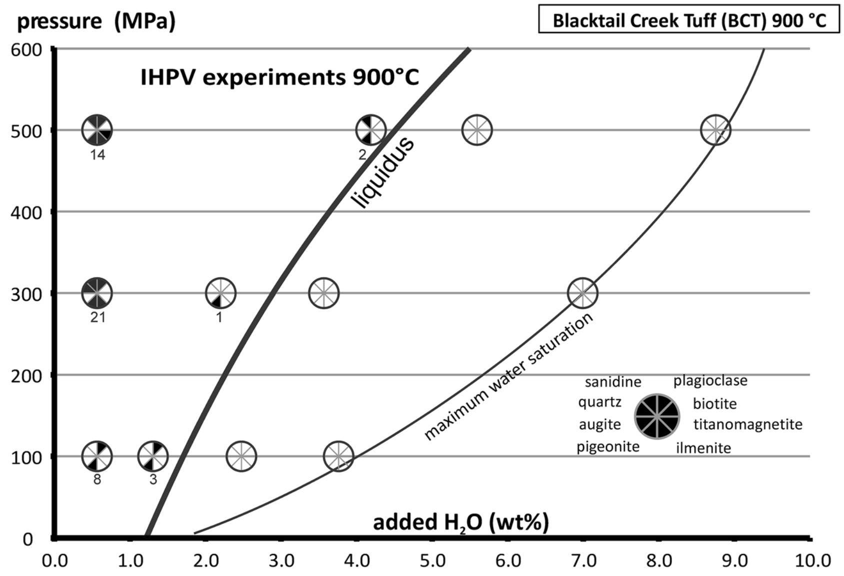

Fig. 10 Phase relations determined for the composition Blacktail Creek Tuff at 900 °C as a function of pressure and added water content in the system (wt% H_2O) at fluid-absent conditions. The experimental data are given in Table 3 and electronic supplement Table 4. The *liquidus line* is determined by our experimental results. The maximum water saturation is determined from the haplogranitic Qz–Ab–Or system. Numbers are given for the degree of crystallization (%) determined by mass balance calculations

addition, partial contamination by the host minerals may not be fully excluded. However, such problems cannot explain some features such as the different compositional groups observed within augites (Fig. 6). Strongly different compositions (Or-rich and Ab-rich) can be observed within one augite mineral. The compositions can also differ strongly from the average matrix glass, which may indicate that minerals crystallized in environments which are different from those just prior to eruption. The trapped glasses in augite have systematically lower FeO concentrations than other glasses (matrix or inclusions in other minerals), and a strong variation in K_2O is observed, with a high number of inclusions having K_2O concentrations higher than 7 wt% and low Na_2O concentrations (<2.5 wt% Na_2O). As discussed above (see results), such variations cannot be explained by contamination from the host mineral during analysis, in particular for alkalis. Several explanations for the formation of high-K inclusions can be proposed. (1) Part of the inclusions was not closed during and after cooling, especially for alkalis, a process that may be coupled with fluid exchange and that has been described in the Snake River Plain magmas. (2) The K-rich inclusions may have been trapped in another magma reservoir which was more evolved (low Fe concentrations) and K-rich. This would imply that some K-rich magmas may occur, at least locally, in the continental crust below the Snake River Plain. However, such K-rich high-silica magmas are not known as eruptive rocks in the Snake River Plain. (3) An alternative is that the augite could crystallize from a biotite breakdown reaction in a rejuvenated initially low-temperature biotite-bearing magma. The composition of melt inclusions could result from local high K concentrations resulting from the biotite breakdown. (4) K-rich inclusions could also be directly formed from partial melting of some K-rich rocks in the continental crust, and in this case, augite present in the magmas would represent restitic phases formed during incongruent melting of a crustal protolith. Following the approach of Chappell (2004), a pelitic source could be expected to obtain such high K_2O concentrations, but augite is not expected to be formed in a metapelitic or K-rich orthogneiss as a product of partial melting (e.g., Vielzeuf and Holloway 1988; Vielzeuf and Montel 1994). (5) Finally, the high K concentration in inclusions may be related to the formation of melt inclusions from a magmatic system at very low water activity, considering that such conditions shift the eutectic compositions to high Or contents. However, this would imply that temperatures were high which contrasts with the low Fe contents. We favor the first and third possible explanations.

The second and third explanations would also be consistent with our experimental and analytical observations, indicating that augite and pigeonite present in the investigated sample may not have been in equilibrium prior to eruption. Temperatures deduced from pyroxene pairs have high uncertainties and differ strongly, depending on the approach that is applied (Table 2). Coexisting pigeonite and augite were not observed in the experimental products. This does not mean that both phases cannot coexist, but it indicates at least that the P–T–XH_2O field at which both phases may coexist is narrow. In the studied sample of Blacktail Creek Tuff, the Aug composition is homogeneous, but other studies emphasized that different populations of pyroxenes may exist in the products of one single eruption (Cathey and Nash 2004; Ellis and Wolff 2012), indicating either that different magmas batches erupted simultaneously or that some pyroxenes with a different origin did not fully re-equilibrate in the erupted magma. In any case, our results confirm that pyroxenes may have complex histories in the Snake River Plain eruptive products.

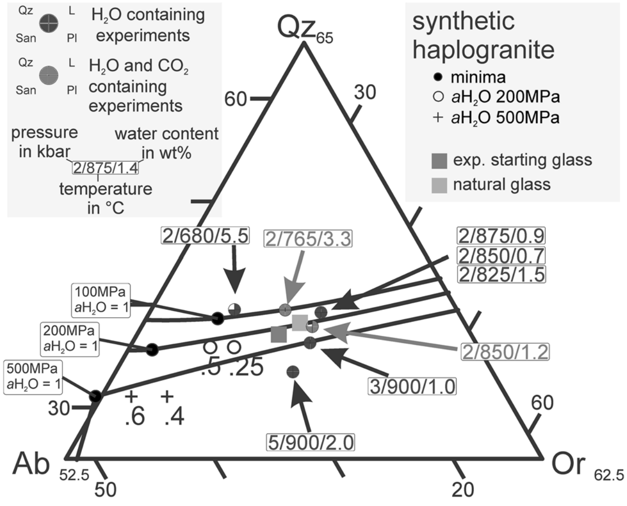

Fig. 11 Ternary Qz–Ab–Or plot of Blacktail Creek Tuff experimental glasses in relationship to cotectic lines in the haplogranitic Qz–Ab–Or system (Holtz et al. 1992). Different conditions and assemblages are labeled and given in the key. Blacktail Creek Tuff glass compositions coexisting with albite, orthoclase and quartz fix the eutectic point for the given condition. Glasses coexisting only with albite and orthoclase represent the cotectic line for both phases

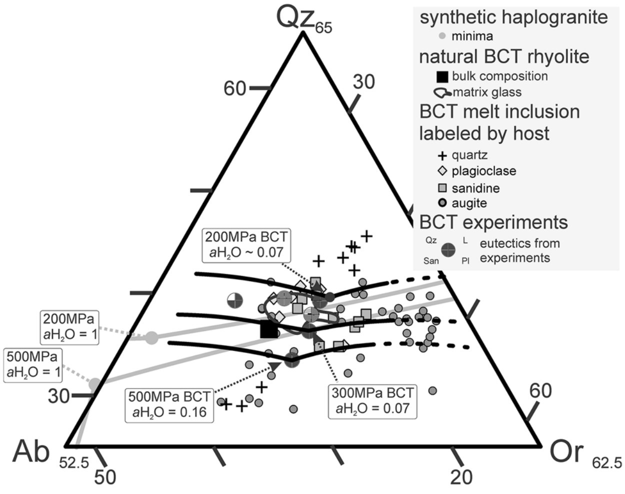

Fig. 12 Ternary Qz–Ab–Or plot of Blacktail Creek Tuff experimental glasses, melt inclusions, matrix glass and bulk composition in relationship to cotectic lines of the haplogranitic Qz–Ab–Or system (Holtz et al. 1992). Curved lines display the estimated cotectic lines together with cotectic points from the experimental results of the Blacktail Creek Tuff system

Conclusion and summary

Our experiments on the natural Blacktail Creek Tuff composition of the Heise eruptive center indicate that the mineral assemblages observed in the natural samples can be only reproduced experimentally if the water concentration in the melt is low (~2.0 ± 0.5 wt% H_2O), assuming temperatures of 845–875 °C (Figs. 8, 9, 10). This temperature range is deduced from the combination of experimental constraints and thermometry. The water content of 2.0 ± 0.5 wt% H_2O is slightly higher than that determined experimentally on Bruneau–Jarbidge magmas which is in the range 0.7–1.3 wt% H_2O (Almeev et al. 2012), assuming a pre-eruptive temperature of 950 °C. Our results demonstrate the general trend of decreasing temperature over time in the Snake River Plain silicic magmatism and are in good agreement with former studies (e.g., Perkins and Nash 2002; Christiansen and McCurry 2008; Bonnichsen et al. 2008; Branney et al. 2008). The depth of magma storage prior to eruption can be fixed at around 3.5–6.5 km (~130–240 MPa) by the combination of our experimental data, the Qz–Ab–Or proportions of the glass matrix and results from the revised Ti-in-quartz geothermobarometer (Huang and Audetat 2012). The interpretation of melt inclusions leads to the conclusion that augite crystals may have a complex history and may not have been in equilibrium with the bulk rock composition of the investigated sample.

Acknowledgments We want to express our appreciation to Eric H. Christiansen and two anonymous reviewers for their critical, thorough reviews and comments improving this paper substantially. We also thank Otto Dietrich and Julian Feige for preparing the thin sections, Eric Wolff and Martin Erdmann for assistance in operating the electron microprobe, Oliver Preuß and Carolin Klahn for technical assistance and Marvin Mätschke and Rebecca Plähn for contributing results of their Bachelor theses. This study was funded by the German Research Foundation (DFG, project Ho 1337/22). Special thanks go to Andreas Audetat for providing quartz standard material to calibrate our microprobe measurements on titanium in quartz.

References

Almeev RR, Bolte T, Nash BP, Holtz F, Erdmann M, Cathey HE (2012) High-temperature, low-H_2O silicic magmas of the Yellowstone hotspot: an experimental study of rhyolite from the Bruneau–Jarbidge eruptive center, Central Snake River Plain, USA. J Petrol 53(9):1837–1866. doi:10.1093/petrology/egs1035

Andersen DJ, Lindsley DH (1985) New (and final!) models for the Ti-magnetite/ilmenite geothermometer and oxygen barometer. Am Geophys Union 66(Abstract AGU 1985 Spring Meeting Eos Transactions):416

Andersen DJ, Lindsley DH, Davidson PM (1993) QUILF: a pascal program to assess equilibria among Fe–Mg–Mn–Ti oxides, pyroxenes, olivine, and quartz. Comput Geosci 19(9):1333–1350

Becker A, Holtz F, Johannes W (1998) Liquidus temperatures and phase compositions in the system Qz–Ab–Or at 5 kbar and very low water activities. Contrib Miner Petrol 130(3):213–224

Bédard JH (2010) Parameterization of the Fe = Mg exchange coefficient (Kd) between clinopyroxene and silicate melts. Chem Geol 274(3–4):169–176

Behrens H, Romano C, Nowak M, Holtz F, Dingwell DB (1996) Near-infrared spectroscopic determination of water species in glasses of the system MAlSi3O8 (M = Li, Na, K): an interlaboratory study. Chem Geol 128(1–4):41–63

Berndt J, Liebske C, Holtz F, Freise M, Nowak M, Ziegenbein D, Hurkuck W, Koepke J (2002) A combined rapid-quench and

H_2-membrane setup for internally heated pressure vessels: description and application for water solubility in basaltic melts. Am Mineral 87(11–12):1717–1726

Bindeman IN, Watts KE, Schmitt AK, Morgan LA, Shanks PWC (2007) Voluminous low $\delta_{18}O$ magmas in the late Miocene Heise volcanic field, Idaho: implications for the fate of Yellowstone hotspot calderas. Geology 35(11):1019–1022

Blundy J, Cashman K (2001) Ascent-driven crystallisation of dacite magmas at Mount St Helens, 1980-1986. Contrib Miner Petrol 140(6):631–650

Bonnichsen B (1982a) The Bruneau–Jarbidge eruptive center, southwestern Idaho. In: Bonnichsen B, Breckenridge RM (eds) Cenozoic geology of Idaho. Idaho Bureau of Mines and Geology Bulletin vol 26, pp 237–254

Bonnichsen B (1982b) Rhyolite lava flows in the Bruneau–Jarbidge eruptive center, southwestern Idaho. In: Bonnichsen B, Breckenridge RM (eds) Cenozoic Geology of Idaho. Idaho Bureau of Mines and Geology Bulletin vol 26, pp 283–320

Bonnichsen B, Citron GP (1982) The Cougar Point Tuff, southwestern Idaho and vicinity. In: Bonnichsen B, Breckenridge RM (eds) Cenozoic Geology of Idaho. Idaho Bureau of Mines and Geology Bulletin vol 26, pp 255–281

Bonnichsen B, Leeman W, Honjo N, McIntosh W, Godchaux M (2008) Miocene silicic volcanism in southwestern Idaho: geochronology, geochemistry, and evolution of the central Snake River Plain. Bull Volc 70:315–342

Botcharnikov RE, Koepke J, Holtz F, McCammon C, Wilke M (2005) The effect of water activity on the oxidation and structural state of Fe in a ferro-basaltic melt. Geochim Cosmochim Acta 69:5071–5085

Branney M, Bonnichsen B, Andrews G, Ellis BS, Barry T, McCurry M (2008) 'Snake River (SR)-type' volcanism at the Yellowstone hotspot track: distinctive products from unusual, high-temperature silicic super-eruptions. Bull Volc 70:293–314

Burnham CW (1994) Development of the Burnham model for prediction of H_2O solubility in magmas. In: Carroll MR, Holloway JR (eds) Volatiles in magmas. Reviews in Mineralogy and Geochemistry 30. Washington: Mineralogical Society of America pp 123–129

Cathey HE, Nash BP (2004) The cougar point tuff: implications for thermochemical zonation and longevity of high-temperature, large-volume silicic magmas of the miocene yellowstone hotspot. J Petrol 45:27–58

Cathey HE, Nash BP (2009) Pyroxene thermometry of rhyolite lavas of the Bruneau–Jarbidge eruptive center, Central Snake River Plain. J Volcanol Geoth Res 188:173–185

Chappell BW (2004) Towards a unified model for granite genesis. Trans R Soc Edinb Earth Sci 95:1–10. doi:10.1017/S0263593300000870

Christiansen RL (2001) The quaternary and pliocene Yellowstone plateau volcanic field of Wyoming, Idaho and Montana: US Geological Survey Professional Paper 729G:145 p

Christiansen EH, McCurry M (2008) Contrasting origins of Cenozoic silicic volcanic rocks from the Western Cordillera of the United States. Bull Volc 70(3):251–267

Clemens JD, Wall VJ (1981) Crystallization and origin of some peraluminous (S-type) granitic magmas. Can Mineral 19:I I lr32

Dall'Agnol R, Scaillet B, Pichavant M (1999) An experimental study of a lower Proterozoic A-type granite from the eastern Amazonian craton, Brazil. J Petrol 40:1673–1698

Drew DL, Bindeman IN, Watts KE, Schmitt AK, Fu B, McCurry M (2013) Crustal-scale recycling in caldera complexes and rift zones along the Yellowstone hotspot track: O and Hf isotopic evidence in diverse zircons from voluminous rhyolites of the Picabo volcanic field, Idaho. Earth Planet Sci Lett 381:63–77

Ellis BS, Wolff JA (2012) Complex storage of rhyolite in the central Snake River Plain. J Volcanol Geoth Res 211–212:1–11

Ellis BS, Barry T, Branney MJ, Wolff JA, Bindeman I, Wilson R, Bonnichsen B (2010) Petrologic constraints on the development of a large-volume, high temperature, silicic magma system: the Twin Falls eruptive centre, central Snake River Plain. Lithos 120:475–489

Ellis BS, Mark DF, Pritchard CJ, Wolff JA (2012) Temporal dissection of the Huckleberry Ridge Tuff: using the 40Ar/39Ar dating technique. Quat Geochronol 9:34–41. doi:10.1016/j.quageo.2012.01.006

Farmer GL, DePaolo DJ (1983) Origin of Mesozoic and Tertiary granite in the western United States and implications for pre-Mesozoic crustal structure: 1. The northern Great Basin. J Geophys Res 88:3379–3410

Fleck RJ, Criss RW (1985) Strontium and oxygen isotopic variations in Mesozoic and Tertiary plutons of central Idaho. Contrib Miner Petrol 90:291–308

Fogel RA, Rutherford MJ (1990) The solubility of carbon dioxide in rhyolitic melts, a quantitative FTIR study. Am Mineral 75:1311–1326

Frost CD, Frost BR (2011) On ferroan (A-type) granitoids: their compositional variability and models of origin. J Petrol 52:39–53

Fuhrman ML, Lindsley DH (1988) Ternary feldspar modeling and thermometry. Am Mineral 73:201–215

Ghiorso MS, Evans BW (2008) Thermodynamics of rhombohedral oxide solid solutions and a revision of the Fe-Ti two-oxide geothermometer and oxygen-barometer. Am J Sci 308:957–1039

Girard G, Stix J (2009) Magma recharge and crystal mush rejuvenation associated with early post-collapse upper basin member rhyolites, yellowstone caldera, wyoming. J Petrol 50:2095–2125

Girard G, Stix J (2010) Rapid extraction of discrete magma batches from a large differentiating magma chamber: the Central Plateau Member rhyolites, Yellowstone Caldera, Wyoming. Contrib Miner Petrol 160:441–465

Harrison TM, Watson EB (1984) The behavior of apatite during crustal anatexis: equilibrium and kinetic considerations. Geochim Cosmochim Acta 48:1467–1477

Holtz F, Pichavant M, Barbey P, Johannes W (1992) Effects of H_2O on liquidus phase relations in the haplogranite system at 2 and 5 kbar. Am Mineral 77:1223–1241

Holtz F, Johannes W, Tamic N, Behrens H (2001) Maximum and minimum water contents of granitic melts generated in the crust: a reevaluation and implications. Lithos 56:1–14

Holtz F, Sato H, Lewis J, Behrens H, Nakada S (2005) Experimental Petrology of the 1991–1995 Unzen Dacite, Japan. Part I: phase relations, phase composition and pre-eruptive conditions. J Petrol 46:319–337

Honjo N, Bonnichsen B, Leeman WP, Stormer JC (1992) Mineralogy and geothermometry of high-temperature rhyolites from the central and western snake river plain. Bull Volc 54:220–237

Huang R, Audetat A (2012) The titanium-in-quartz (TitaniQ) thermobarometer: a critical examination and re-calibration. Geochim Cosmochim Acta 84:75–89. doi:10.1016/j.gca.2012.01.009

James RS, Hamilton DL (1969) Phase relations in the system $NaA1Si_3O_8$–$KA1Si_3O_8$–$CaA1_2Si_2O_8$–SiO_2 at 1 kilobar water vapour pressure. Contrib Miner Petrol 21:111–141

Klimm K, Holtz F, Johannes W, King PL (2003) Fractionation of metaluminous A-type granites: an experimental study of the Wangrah Suite, Lachlan Fold Belt, Australia. Precambr Res 124:327–341

Klimm K, Holtz F, King PL (2008) Fractionation versus magma mixing in the Wangrah Suite A-type granites, Lachlan Fold Belt, Australia: experimental constraints. Lithos 102(3–4):415–434

Leeman WP, Oldow JS, Hart WK (1992) Lithosphere-scale thrusting in the western U.S. Cordillera as constrained by Sr and Nd isotopic transitions in Neogene volcanic rocks. Geology 20:63–66

Leeman WP, Annen C, Dufek J (2008) Snake River Plain—Yellowstone silicic volcanism: implications for magma genesis and magma fluxes. Geol Soc Lond Spec Publ 304:235–259

Lindsley DH (1983) Pyroxene thermometry. Am Mineral 68:477–493

Mandeville CW, Webster JD, Rutherford MJ, Taylor BE, Timbal A, Faure K (2002) Determination of molar absorptivities for infrared absorption bands of H_2O in andesitic glasses. Am Mineral 87:813–821

McCurry M, Rodgers DW (2009) Mass transfer along the Yellowstone hotspot track I: petrologic constraints on the volume of mantle-derived magma. J Volcanol Geoth Res 188:86–98

Moore G, Vennemann T, Carmichael ISE (1998) An empirical model for solubility of H_2O in magmas to 3 kilobars. Am Mineral 83:36–42

Morgan LA, McIntosh WC (2005) Timing and development of the Heise volcanic field, Snake River Plain, Idaho, western USA. Geol Soc Am Bull 117:288–306

Naney MT (1983) Phase equilibria of rock forming ferromagnesian silicates in granitic systems. Am J Sci 283:993–1033

Nash BP, Perkins ME, Christensen JN, Lee DC, Halliday AN (2006) The Yellowstone hotspot in space and time: Nd and Hf isotopes in silicic magmas. Earth Planet Sci Lett 247:143–156

Parat F, Holtz F (2005) Sulfur partition coefficient between apatite and rhyolite: the role of bulk S content. Contrib Miner Petrol 150:643–651

Parat F, Holtz F, Feig S (2008) Pre-eruptive conditions of the Huerto andesite (Fish Canyon System, San Juan Volcanic Field, Colorado): influence of volatiles (C-O-H-S) on phase equilibria and mineral composition. J Petrol 49:911–935

Perkins ME, Nash BP (2002) Explosive silicic volcanism of the Yellowstone hotspot: the ash fall tuff record. Geol Soc Am Bull 114:367–381

Pichavant M (1987) Effects of B and H_2O on liquidus phase relations in the haplogranitic system at 1 kbar. Am Mineral 72:1056–1070

Pichavant M, Costa F, Burgisser A, Scaillet B, Martel C, Poussineau S (2007) Equilibration scales in silicic to intermediate magmas: implications for experimental studies. J Petrol 48(10):1955–1972

Putirka KD (2008) Thermometers and barometers for volcanic systems. Rev Mineral Geochem 69(1):61–120

Puziewicz J, Johannes W (1988) Phase equilibria and compositions of Fe–Mg–Al minerals and melts in water-saturated peraluminous granitic systems. Contrib Miner Petrol 100:156–168

Rutherford MJ, Sigurdsson H, Carey S, Davis A (1985) The May 18, 1980, eruption of Mount St. Helens. 1. Melt composition and experimental phase equilibria. J Geophys Res 90:2929–2947

Scaillet B, Evans BW (1999) The 15 June 1991 eruption of mount Pinatubo. I. Phase equilibria and pre-eruption P-T-fO2-fH2O conditions of the dacite magma. J Petrol 40:381–411

Scaillet B, Pichavant M, Roux J (1995) Experimental crystallization of leucogranite magmas. J Petrol 36:663–705

Schuessler JA, Botcharnikov RE (2008) Amorphous materials: properties, structure, and durability: oxidation state of iron in hydrous phono-tephritic melts. Am Mineral 93(10):1493–1504

Stormer JC Jr (1983) The effects of recalculation on estimates of temperature and oxygen fugacity from analyses of multicomponent iron-titanium oxides. Am Mineral 68:586–594

Tamic N, Behrens H, Holtz F (2001) The solubility of H_2O and CO_2 in rhyolitic melts in equilibrium with a mixed CO_2–H_2O fluid phase. Chem Geol 174:333–347

Tuttle OF, Bowen NL (1958) Origin of granite in the light of experimental studies in the system $NaAlSi_3O_8$–$KAlSi_3O_8$–SiO_2–H_2O. Geol Soc Am Memoir 74:153 p

Vazquez JA, Kyriazis SF, Reid MR, Sehler RC, Ramos FC (2009) Thermochemical evolution of young rhyolites at Yellowstone: evidence for a cooling but periodically replenished postcaldera magma reservoir. J Volcanol Geoth Res 188:186–196

Vielzeuf D, Holloway JR (1988) Experimental determination of the fluid-absent melting relations in the pelitic system: consequences for crustal differentiation. Contrib Miner Petrol 98(3):257–276

Vielzeuf D, Montel JM (1994) Partial melting of metagreywackes: part 1, fluid-absent experiments and phase relationships. Contrib Miner Petrol 117(4):375–393

Watson EB, Harrison TM (1983) Kinetics of zircon dissolution and zirconium diffusion in granitic melts of variable water content. Contrib Miner Petrol 84:66–72

Watts KE, Bindeman IN, Schmitt AK (2011) Large-volume rhyolite genesis in caldera complexes of the Snake River Plain: insights from the Kilgore Tuff of the Heise volcanic field, Idaho, with comparison to Yellowstone and Bruneau–Jarbidge rhyolites. J Petrol 52:857–890

Whitney JA (1988) The origin of granite: the role and source of water in the evolution of granitic magmas. Geol Soc Am Bull 100:1886–1897

Whitney DL, Evans BW (2010) Abbreviations for names of rock-forming minerals. Am Mineral 95:185–187

Withers AC, Behrens H (1999) Temperature-induced changes in the NIR spectra of hydrous albitic and rhyolitic glasses between 300 and 100 K. Phys Chem Miner 27:119–132

Wyllie PJ (1971) A discussion of water in the crust. In Heacock JG (ed) the structure and physical properties of the earth's crust. Geophysical Monograph 14, American Geophysical Union, Washington, pp 257–260